



Dedicated to innovation in aerospace

COMPANY CONFIDENTIAL

NLR-TR-2016-504 |

Evaluation of The Use of Deconvolution Algorithms for Determination of Trailing Edge Noise Levels

CUSTOMER: Netherlands Aerospace Centre

NLR – Netherlands Aerospace Centre



Netherlands Aerospace Centre

NLR is a leading international research centre for aerospace. Bolstered by its multidisciplinary expertise and unrivalled research facilities, NLR provides innovative and integral solutions for the complex challenges in the aerospace sector.

NLR's activities span the full spectrum of Research Development Test & Evaluation (RDT & E). Given NLR's specialist knowledge and facilities, companies turn to NLR for validation, verification, qualification, simulation and evaluation. NLR thereby bridges the gap between research and practical applications, while working for both government and industry at home and abroad.

NLR stands for practical and innovative solutions, technical expertise and a long-term design vision. This allows NLR's cutting edge technology to find its way into successful aerospace programs of OEMs, including Airbus, Embraer and Pilatus. NLR contributes to (military) programs, such as ESA's IXV re-entry vehicle, the F-35, the Apache helicopter, and European programs, including SESAR and Clean Sky 2.

Founded in 1919, and employing some 650 people, NLR achieved a turnover of 73 million euros in 2014, of which three-quarters derived from contract research, and the remaining from government funds

For more information visit: www.nlr.nl



Dedicated to innovation in aerospace

COMPANY CONFIDENTIAL

NLR-TR-2016-504 |

Evaluation of The Use of Deconvolution Algorithms for Determination of Trailing Edge Noise Levels

CUSTOMER: Netherlands Aerospace Centre

AUTHOR(S):

H.D.T. Klein

Netherlands Aerospace Centre

No part of this report may be reproduced and/or disclosed, in any form or by any means without the prior written permission of NLR.

CUSTOMER	Netherlands Aerospace Centre
CONTRACT NUMBER	
OWNER	
DIVISION NLR	Aerospace Vehicles
DISTRIBUTION	Limited
CLASSIFICATION OF TITLE	COMPANY CONFIDENTIAL

APPROVED BY :		
AUTHOR	REVIEWER	MANAGING DEPARTMENT
H.D.T. Klein		
DATE	DATE	DATE

Summary

This report covers the evaluation of an extension of the CLEAN-SC algorithm to measure trailing edge noise. For wind turbines noise is often a limiting factor in both placement and maximum rotating speed. Hence, the reduction of noise is of great interest for the sustainable energy sector.

One of the most dominating mechanisms for wind turbines is the airfoil noise originating from the trailing edge. This noise can be reduced by the use of so called serrations. Multiple experiments have been conducted to confirm the effective working of serrations. Also in 2014 an experiment on the use of serrations was conducted at the NLR.

It is difficult to obtain qualitative good measurements of trailing edge noise because of the presence of spurious noise sources. These spurious noise sources often have known locations such as the noise originating from the junctions between the tested airfoil and the endplates in a wind tunnel caused by the boundary layer and the arising of horse shoe vortices.

With previously used methods such as the use of microphone array and conventional beamforming it is difficult to distinguish these noise sources and measure them individually. However, in 2015 an extension of the CLEAN-SC algorithm was developed which was able to distinguish the noise sources and measure solely the noise originating from the trailing edge.

This method was tested on a single case. To evaluate the algorithm, the acoustic data from the experiment in 2014 is now processed using the extended algorithm. The algorithm proved to be effective in the determination of trailing edge noise. Although the iterative deconvolution based on the empirical point spread function was not able to obtain robust physical results, the first deconvolution step by linear regression based on theoretical PSF was very effective.

The new algorithm was able to accurately determine trailing edge noise above 1 kHz. In comparison with the previously used method, the trailing edge noise was lower and more accurate the frequency ranges below 4000 Hz. This was because the old method overestimated the trailing edge noise in that range due to the spurious corner sources and the limited resolution. The leading edge sources that were filtered out turned out to be independent of the use of serrations and the trailing edge noise data showed a good collapse when scaling rules are applied. This confirmed the validity of the algorithm. The algorithm was then applied on the complete set of cases to get to obtain new data on the performance of the serrations. According to the new method the best serrations, namely the flexible serrations, seemed to cause an average noise reduction of 6 dB compared to 4.6 dB according to the previously used method to measure TE noise.



Contents

Abbreviations	7
1 Introduction	9
1.1 Trailing Edge Noise	9
1.2 Measurements of Trailing Edge Noise	9
1.3 Objectives	10
1.4 Outline	10
2 Beamforming theory	12
2.1 Conventional beamforming	12
2.2 CLEAN 13	
2.3 CLEAN-SC	15
2.4 Extended CLEAN-SC algorithm for TE noise	15
3 Experimental Setup	17
4 Results and Discussion	18
4.1 Optimizing Method	18
4.1.1 Regression fit	18
4.1.2 Microphone setup	20
4.1.3 CLEAN step	21
4.2 Source Decomposition	22
4.3 Scaling ²²	
4.4 Comparison with old results	24
4.5 Use of Serrations	25
5 Conclusions and Recommendations	26
6 Figures	27
7 References	59

Abbreviations

ACRONYM	DESCRIPTION
DNW	German-Dutch Wind Tunnels
NLR	Netherlands Aerospace Centre
TBL-TE	Turbulent boundary layer trailing edge
TE	Trailing edge
LE	Leading edge
CB	Conventional Beamforming
KAT	Small anechoic wind tunnel
AoA	Angle of attack
US-TOP	Uncut serrations mounted on the suction side
US-BOT	Uncut serrations mounted on the pressure side
FS	Flexible serrations
std	Standard deviation
PSF	Point source function
CSM	Cross-Spectral matrix
PWL	Sound Power Level

This page is intentionally left blank.

1 Introduction

1.1 Trailing Edge Noise

With aircraft engines getting quieter, the self-noise of airplanes and airfoils is becoming a more important topic. The damping of airfoil self-noise is also of great significance to the wind turbine industry. Due to laws and regulations, the noise produced by wind turbines is one of the main issues and restraining factors on the placement of wind turbines. Likewise, wind turbine noise often restricts the maximum rotational speed. Hence reducing the noise coming from the blades can be of great contribution to the wind energy industry and thereby to the sustainable energy sector.

Noise produced by wind turbines is mainly produced by the self-noise of airfoils. For the self-noise of airfoils, multiple mechanisms are responsible. However, at high Reynolds number R_c , which is the case for wind turbines, the dominant mechanism is the so called, *turbulent boundary layer trailing edge* (TBL-TE) noise.

A promising tool in order to reduce this trailing-edge (TE) noise is to mount serrations on the trailing edge. According to Howe this will reduce the span wise length producing noise. In another study, Howe predicted that for the use of saw tooth serrations, noise would reduce according to $10\log[1+4h/\lambda^2]$ for the frequencies $\omega h/U \gg 1$, where λ is the serrations width, ω is the acoustic frequency, h the saw tooth amplitude and U the flow speed. Hence the noise reduction was claimed to be dependent on the amplitude width ratio of the serrations.

Several experimental studies confirmed that saw tooth serrations indeed cause noise reduction. However, it was also found that at high frequency range, the noise increases,. Gruber et al , did extensive experiments on an NACA6512 airfoil and stated that the increasing or decreasing of noise was dependent on the so called Strouhal number $S_{t_\delta} = f\delta/U$ with f being frequency in Hz and δ being the boundary layer thickness. Above $S_{t_\delta} \approx 1$ noise would increase and below, the noise would decrease. Gruber also mentioned that noise decrease was more dependent on (h/δ) than on (λ/h) . It should be at least $h/\delta > 0.5$ and reaches a maximum efficiency when $h/\delta = 2$. Gruber tested serrations in the range of $\lambda = 1.5 - 12.5 \text{ mm}$ and it showed that narrow serrations performed better than wider serrations. This was also confirmed in other studies,. Braun argued that the serrations should be aligned with the flow angle at the trailing edge. This should reduce high pitch noise caused by un aligned serrations. In short: long, narrow serrations are favored and these serrations should be aligned with the flow angle.

1.2 Measurements of Trailing Edge Noise

In wind tunnel experiments, one of the difficulties is to measure pure TE noise due to the presence of spurious noise sources such as background noise or sources at the junctions between the airfoil and the endplates. For example, extra spurious noise arises at the leading edge and the trailing edge corners of the airfoil due to the boundary layer and the arising of horse shoe vortices.

To measure TE noise single microphones or a microphone array in a line or in a surface are often used. The latter technique is known as beamforming and is able to provide a source map on which different noise sources can be distinguished. However, the resolution of these source maps is limited, especially for low frequencies. Therefore, it is difficult to filter out spurious noise and accurately measure TE noise source in term of radiated noise per unit length.

To improve the resolution of source maps, deconvolution methods like DAMAS, CLEAN and CLEAN-SC have been developed. Deconvolution methods determine theoretical or empirical contributions of point sources to the source map or cross-spectral matrix. Those contributions are subtracted from the original map and replaced with clean representations of sources. Since the locations of the sources are not known, CLEAN and CLEAN-SC search for the maximum point in a source map, assume that a source is located at that location and 'clean' the source from the map. Then a next maximum is located and the same step is repeated in an iterative process. Detailed theory of beamforming techniques will be discussed in chapter 2.

The disadvantages of these algorithms are that a source can be placed at some point where no actual source is located. Especially for TE noise, where the source of interest has the shape of a line, this results into inaccurate outcomes. In 2015 Tuinstra and Sijtsma developed an extension of the CLEAN-SC algorithm where the source distribution, based on physical knowledge, is given as input. This makes it possible to solve a system of equations for all the sources at the same time. After that an extended CLEAN-SC algorithm is used to 'clean' the source map. This algorithm was tested on one specific case and showed good results.

1.3 Objectives

In 2014, an experimental investigation on the use of serrations was conducted by David E. Falerios. In this study a microphone array was used to research different configurations of serrations. To obtain results the mid span point on the trailing edge was taken for the sound power level (PWL). This was sufficient to draw conclusions on the performance of the serrations but further investigation on the acoustic data was left out.

The main goal of this study is to evaluate the extension on the CLEAN-SC algorithm with the use of acoustic data from Falerios' experiment. In order to do so, the following research questions will be answered:

- How does the extension of CLEAN-SC perform?
- What is the power level of the spurious noise sources compared to the TE noise?
- Are the spurious sources filtered out properly?
- Can scaling rules from literature be applied to the obtained TE noise spectra?
- What is the difference in Trailing Edge noise estimation compared to the old method?
- Are the conclusions of the previous conducted experiment still valid?

1.4 Outline

The outline of this report is as following. First, the beamforming theory is explained in order to obtain an understanding of the principles used in this study. In the next chapter the experimental setup is laid out to get a hold on the experimental research that was conducted before. After that, the results are presented and discussed. In the last chapter, the conclusion and recommendations are presented. To maintain overview, figures are presented in a separated chapter. After that the reference list can be found.

2 Beamforming theory

In this chapter, the beamforming theory will be explained in order to enlarge the understanding of the techniques used. First the basic principles are explained leading to the most common beamforming method Conventional Beamforming (CB). This method will be expanded to CLEAN and CLEAN-SC respectively which eventually will lead to the extension used in this study. The notation and explanation of Sijtsma and Tuinstra will be closely followed. For more details, one is referred to the literature.

2.1 Conventional beamforming

Consider n microphones which measured noise transformed in complex amplitudes in the frequency domain.

$$\mathbf{p}(f) = \begin{pmatrix} p_1(f) \\ p_2(f) \\ \vdots \\ p_n(f) \end{pmatrix} \quad (1)$$

The cross-spectral matrix (CSM) is defined as:

$$C = \frac{1}{2} \mathbf{p} \mathbf{p}^* \quad (2)$$

Now a steering vector is defined which represents the signal of a unit monopole source:

$$\mathbf{g}_n = \frac{-e^{2\pi i f \Delta t_e(x_n, \xi)}}{4\pi \sqrt{(\mathbf{M} \cdot (\mathbf{x}_n - \xi))^2 + \beta^2 \|\mathbf{x}_n - \xi\|^2}} \quad (3)$$

With \mathbf{M} being the Mach vector, $\beta^2 = 1 - |\mathbf{M}|^2$ and $\Delta t_e(x_n, \xi)$ being the time delay:

$$\Delta t_e = \frac{1}{c\beta^2} \left(-\mathbf{M} \cdot (\mathbf{x}_n - \xi) + \sqrt{\mathbf{M} \cdot (\mathbf{x}_n - \xi) + \beta^2 \|\mathbf{x}_n - \xi\|^2} \right) \quad (4)$$

Here \mathbf{x}_n denotes the location of the microphone and ξ denotes the location of a scan point looked in to. The aim is to find the complex amplitude of each location by comparing the pressure vector \mathbf{p} with the steering vector \mathbf{g} this is done by the minimisation of

$$J = \|\mathbf{p} - a\mathbf{g}\|^2 \quad (5)$$

With solution

$$a = \frac{\mathbf{g}^* \mathbf{p}}{\|\mathbf{g}\|^2} \quad (6)$$

or notated as auto power

$$A = \frac{1}{2} |a|^2 = \frac{\mathbf{g}^* C \mathbf{g}}{\|\mathbf{g}\|^4} = \mathbf{w}^* C \mathbf{w} \quad (7)$$

with weighting vector:

$$\mathbf{w} = \frac{\mathbf{g}}{\|\mathbf{g}\|^2} \quad (8)$$

The application of these equations will result in a source map which is known as Conventional Beamforming. This method is a common used technique and was programmed with Matlab. An example of a 2D source map is shown in *Figure 1*. As it can be seen a single source returns a peak on the source maps and also some other peaks called side lobes can be observed. The width of the peak 3 dB below the top defines the resolution and can be estimated with the following empirical relation.

$$Resolution = 425 \frac{Y}{Df} \quad (9)$$

Y and D denote the distance to the source and the diameter of the array respectively and f denotes the frequency. For a normal array as used in the wind tunnel experiment where the distance and diameter are 0.6 and 0.8 meter, at 2000 and 1000 Hz, the resolution will be 16 and 32 cm respectively. For these low frequencies the resolutions are quite poor and since the tested airfoil is only 50 cm wide it will become more difficult to distinguish different sources from each other. Variances on CB such as Minimum Variance, Robust Adaptive Beamforming and Functional Beamforming can be applied to improve the resolution, but to effectively tell apart the sources of interest and the spurious sources, deconvolution algorithms such as DAMAS, CLEAN and CLEAN-SC have to be used. DAMAS is not considered. CLEAN and CLEAN-SC will be discussed in the section below.

2.2 CLEAN

The CLEAN algorithm searches source locations, then subtracts the theoretical contributions of these sources from the CSM and replaces them with a clean point in an iterative process. Suppose there is a unit source in a scan point ξ_k . This source induces a CSM given by:

$$\mathbf{G}_k = \mathbf{g}_k \mathbf{g}_k^* \quad (10)$$

According to the theory the source will contribute to source powers in scan points ξ_j

$$A_{kj} = \mathbf{w}_j^* \mathbf{G}_k \mathbf{w}_j \quad (11)$$

This expression is known as the Point Spread Function (PSF), which describes the theoretical response of a point source on the source map. To locate the source, the CLEAN algorithm searches for the maximum peak and determines the corresponding scaled PSF

$$A_{max,j} = \mathbf{w}_j \mathbf{G}_{max} \mathbf{w}_j^* \quad (12)$$

where \mathbf{G}_{max} is the CSM induced by the source in ξ_{max}

$$\mathbf{G}_{max}^{(i)} = A_{max}^{(i-1)} \mathbf{g}_{max} \mathbf{g}_{max}^* \quad (13)$$

The CSM is subtracted from the current CSM and results in a degraded CSM which can be written as a single iterative step:

$$\mathbf{C}^{(i)} = \mathbf{C}^{(i-1)} - \mathbf{G}^{(i)} \quad (14)$$

The new 'dirty' map is formed by:

$$A_j^{(i)} = A_j^{(i-1)} - w_j^* G_{\max}^{(i)} w_j \quad (15)$$

This step can be repeated until a certain stop criterion is reached, for example.

$$\|c^{(i+1)}\| \geq \|c^{(i)}\| \quad (16)$$

This is the point where the degraded CSM contains more information than the previous CSM. After this process, a clean map can be formed by summing the clean beams and the remaining 'dirty' map.

$$A_j = \sum_{i=1}^I Q_j^{(i)} + A_j^{(I)} \quad (17)$$

Here is $Q_j^{(i)}$ the replacing clean beam for the PSF

$$Q_j^{(i)} = A_{\max}^{(i-1)} 10^{-\lambda |\xi_j - \xi_{\max}^{(i)}|^2} \quad (18)$$

where λ is a parameter to determine the width of the beam. Often a safety loop gain is used ($0 < \varphi \leq 1$) replacing equations (14) and (18):

$$\begin{cases} c^{(i)} = c^{(i-1)} - \varphi A_{\max}^{(i-1)} g_{\max}^{(i)} g_{\max}^{*(i)} \\ Q_j^{(i)} = \varphi A_{\max}^{(i-1)} 10^{-\lambda |\xi_j - \xi_{\max}^{(i)}|^2} \end{cases} \quad (19)$$

This above described algorithm can be summarized in the following steps:

1. Obtain a 'dirty' source map with CB.
2. Find the peak location in the map.
3. Subtract the corresponding PSF from the 'dirty' source map.
4. Repeat step 2 and 3 until a stop criterion is reached.
5. Replace the subtracted PSF's with the 'clean beams' to obtain a clean map.

The CLEAN algorithm can provide clear maps than the conventional methods. However, the assumption is made that there is uniform source directivity and no loss of coherence in order to use steering vector g to describe the sound transfer. These assumptions are seldom fulfilled in aero-acoustic measurements. Dealing with this leads to CLEAN-SC algorithm.

2.3 CLEAN-SC

Instead of using the original PSF function, the CLEAN algorithm based on Spatial Coherence makes use of the fact that the side lobes in a source plot are coherent with the main lobe. Therefore, use is made of source cross-power. This is defined as

$$B_{jk} = \mathbf{w}_j^* \mathbf{C} \mathbf{w}_k \quad (20)$$

In the case of CLEAN-SC now another choice is made for the matrix $\mathbf{G}^{(i)}$. It is demanded that the source cross-powers of any point ξ_j with the peak location ξ_{max} are determined entirely by $\mathbf{G}^{(i)}$. Therefore,

$$\mathbf{w}_j^* \mathbf{C}^{(i-1)} \mathbf{w}_{max} = \mathbf{w}_j^* \mathbf{G}^{(i)} \mathbf{w}_{max} \quad (21)$$

This is satisfied when:

$$\mathbf{C}^{(i-1)} \mathbf{w}_{max} = \mathbf{G}^{(i)} \mathbf{w}_{max} \quad (22)$$

This does not directly lead to a unique solution for $\mathbf{G}^{(i)}$, but if the induced CSM is written into the form

$$\mathbf{G}^{(i)} = \mathbf{A}_{max}^{(i-1)} (\mathbf{h}^{(i)} \mathbf{h}^{*(i)} - \mathbf{H}^{(i)}) \quad (23)$$

where $\mathbf{H}^{(i)}$ contains the diagonal elements of $\mathbf{h}^{(i)} \mathbf{h}^{*(i)}$. The solution for (22) is then

$$\mathbf{h}^{(i)} = \frac{1}{(1 + \mathbf{w}_{max}^{*(i)} \mathbf{H}^{(i)} \mathbf{w}_{max}^{(i)})^{\frac{1}{2}}} \left(\frac{\mathbf{C}^{(i-1)} \mathbf{w}_{max}^{(i)}}{A_{max}^{(i-1)}} + \mathbf{H}^{(i)} \mathbf{w}_{max}^{(i)} \right) \quad (24)$$

As this is an implicit expression which can be solved iteratively. Furthermore, the iterative CLEAN-SC process operates analogously to equation (19).

$$\begin{cases} \mathbf{C}^{(i)} = \mathbf{C}^{(i-1)} - \varphi A_{max}^{(i-1)} \mathbf{h}^{(i)} \mathbf{h}^{*(i)} \\ Q_j^{(i)} = \varphi A_{max}^{(i-1)} 10^{-\lambda} |\xi_j - \xi_{max}^{(i)}|^2 \end{cases} \quad (25)$$

This is already a good method to distinguish noise sources from each other. But the method is not very suitable for TE noise. The goal of analyzing the trailing edge noise measurements in this study is to obtain a line source along the TE and to distinguish it from the other spurious noise sources. Adapting the algorithm will make it suitable for TE noise.

2.4 Extended CLEAN-SC algorithm for TE noise

In 2015 Tuinstra developed a CLEAN-SC extension which makes use of predefined source locations. Because the locations of the noise sources are known, it is possible to find the source powers quite accurate.

First, it is assumed that there are m monopole sources of which the location is known. They are representing the line source at the trailing edge and other known spurious noise sources. If Z is the subset of indices of scan points at source locations and it is assumed that there are no other significant sources, then the CSM induced by a point source at $\xi_j, j \in Z$ is

$$\mathbf{G}_j' = \mathbf{C} - \frac{1}{2} \sum_{k \in Z \setminus \{j\}}^{m-1} \mathbf{g}_k \mathbf{g}_k^* S_k \quad (26)$$

Here is S_k the source auto-power of the source at sub-PSF resolution. These source auto-powers can be found by solving the system of equations based on theoretical PSF:

$$A_j = \frac{1}{2} \sum_{k \in Z}^n \mathbf{w}_j^* \mathbf{g}_k \mathbf{g}_k^* \mathbf{w}_j S_k \quad (27)$$

By selecting a set of points j (fit points) an overdetermined system of equations is obtained and can be solved by means of linear least-squares regression. The system is further restricted by demanding that the source elements at the trailing edge should be of equal sound power. This results in a first estimate of the source powers which is called the regression fit. The auto power A_j' on \mathbf{G}_j' is derived from CB and then the steering vector \mathbf{h} can be derived from

$$\mathbf{h} = \frac{1}{(1 + \mathbf{w}_j^* \mathbf{H} \mathbf{w}_j)^{\frac{1}{2}}} \left(\frac{\mathbf{G}_j' \mathbf{w}_j}{A_j'} + \mathbf{H} \mathbf{w}_j \right) \quad (28)$$

The PSF then follows from equation (11) and

$$\mathbf{G}_j = A_j' (\mathbf{h} \mathbf{h}^* - \mathbf{H}) \quad (29)$$

Summarizing, the extended CLEAN-SC algorithm for TE noise consist of the following steps:

1. Apply CB to the CSM to obtain a source map.
2. Estimate the source auto-powers S_j of the line source and other spurious noise sources by solving equation (27) by means of least square regression.
3. Select a source location ξ_j from the known sources and determine the reduced CSM \mathbf{G}_j' from equation (26) .
4. Determine \mathbf{h} and the corresponding matrix \mathbf{G}_j .
5. Replace the CSM: $\mathbf{C} = \mathbf{C} - \varphi \mathbf{C}_j$ and remove the scan point index j from subset Z
6. Return to step 3, until all line source elements and spurious sources have been removed from the CSM, then the original CLEAN-SC algorithm can be applied on the remaining CSM.
7. After this the source map can be reconstructed with the source auto-powers.

To see how the extended algorithm performs, a simulation of the test setup is analyzed. (The experimental setup will be explained in the next chapter.) The TE noise is simulated as a line of equally strong point sources (see Figure 2), on the LE corners, source points of 16 times the strength of the TE are placed and on the TE corners the simulated sources have 64 and 36 times the strength of the TE. To simulate a real situation, the LE corner sources are given as sources for the algorithm. The conventional beamforming and clean source maps are given in Figure 3 and 4. As can be seen, the spurious sources are filtered out effective. A power spectrum is given in Figure 5. Also the regression fit can be used to find the source powers. Both regression fit and the clean solution show proper results i.e. within 1 dB off the real source power. Below 1 kHz the algorithm develops difficulties determining the source power. In practice it will also become clear that the algorithm is no longer able to distinguish the sources. Also, in a simulation no coherence loss and no disturbance on the CSM due to the end plates will occur.

3 Experimental Setup

In this section, the setup will be discussed. For more extensive details and motivations, one is referred to the original report on the experiment.

The measurements were conducted at the NLR's Small Anechoic Wind Tunnel KAT. The KAT is an open circuit, open jet wind tunnel, with a nozzle of 0.51 x 0.38 m. Two parallel end plates (0.90 x 0.70 m²) are connected to provide a semi-open test section. In this section, a DU-96-W-180 airfoil was fixed in a vertical position, spanning between the two plates. (Figure 6) The room of 5x5x3 m³, surrounding the test section, was completely covered with 0.5 foam wedges. (Figure 7) This yields more than 99% absorption above 500 Hz.

The acoustic measurements were performed, using an array of 48 microphones located at the suction side of the airfoil at a distance of 0.6 m from the center of the KAT wind tunnel. Dimensions were 0.6 x 0.8 m² (Figure 8). The scan surface for noise surfaces had its origin located at mid span in the rotating axis of the airfoil which is 31.3% c from the leading edge, the scan surface rotates with the airfoil. (Figure 9) The x-axis is in the direction of the airfoil chord line, the y-axis perpendicular to that and the z-axis is upwards positive in the span wise direction of the airfoil.

Also distinction was made between the geometric AoA and the effective AoA, due to the fact that the measurements were conducted in an open wind tunnel. (See also Figure 9) The measurements were conducted at different AoA's but the AoA's used in this report are with geometric AoA 0, 10.51 and 14.37, which correspond with effective AoA 0, 6 and 8.2. The latter AoA corresponds with the specific wind turbine section ($r/R = 0.9$) producing the most noise.

During the measurements flow velocities of 40, 50, 60 and 70 m/s were used. The serrations were mounted on the entire trailing edge with dimensions: $h = 15$ mm and $\lambda = 7.5$ mm. There were six different configurations of serrations made and tested. The first configuration was a clean unserrated edge. The second and third configurations were just serrations with a fixed angle to align with the flow at AoA = 14.37. One mounted on the suction side (TOP) and one mounted on the pressure side (BOT). These are the so called uncut serrations since no cut were made in the steel plate to make it flexible. This was actually done for the fourth and the fifth configurations. A cut section in the plate was added to make the serrations flexible and thus able to align with the flow. However, in this report these two serrations will not be mentioned further since they did not perform well because of the disturbance of the flow caused by the cuts. The sixth configuration was a serration with a flexible joint between the serrations and airfoil also covering the transition maintaining a smooth flow. Hence it could align with the flow but the disadvantages of the cut serrations were overcome. (FS)

4 Results and Discussion

In this section the results from the acoustic data processing are presented and discussed. First a survey is conducted to find optimal approach and successfully obtain TE noise data. This starts with trying to find the optimal source distribution for a regression fit. Then the microphone weighting will be conducted and to conclude the CLEAN deconvolution step will be applied.

When the right approach is selected the first result can be analysed. The spurious sources will be studied first. Secondly, scaling rules will be applied to evaluate the scaling of the measured TE noise. Then the comparison will be made with old results to see what the differences are. In the end the noise reduction performances of the serrations will be presented to confirm the conclusions made in the previous conducted experiment.

4.1 Optimizing Method

4.1.1 Regression fit

In the regression fit, i.e. solving equation (27), a possible obtained distribution based on the point spread function is given. To evaluate the outcome of the regression fit, source maps are generated based on a simulated CSM using the regression fit source powers. The simulated source map is then compared to the measured source map. The case chosen to use for the evaluation is a clean TE at 0 AoA with flow velocity 70 m/s. In Figure 10 such a comparison is illustrated for a specific source distribution and regression fit at 1475 Hz where it was assumed that LE and TE corners would act as single independent point sources.

However, multiple setups with different source distributions and fit points selected were tested and it was found that assuming line sources along both the LE and TE corners of independent sources resulted into the best regression fits. Figure 11 shows such a distribution. This can also be explained when looking to the actual flow. Figure 12 represents a flow visualization near the end plate. On the end plate a boundary layer is present in the flow. As this boundary layer encounters the LE, vortices arise and move over the airfoil to the TE. Hence the flow is influenced by the end plate not only at the single points on the end plate but also on the edge near the end plate.

Different lengths and fit points have been examined. The first set of fit points are a vertical line along the TE, 3 horizontal lines: at $z = -0.25$, at $z = 0$ and $z = 0.25$ m and 2 vertical lines on the LE corners (Figure 13). The other set of fit points tested were all the points within a rectangle around the airfoil. To make proper judgement on the similarity of the simulated source map and the measured source map, a single evaluation point in the source map was chosen to represent the power level of the trailing edge. This point was chosen to be on the trailing edge 4 cm below the mid span point to be located in between the two corner sources. (Figure 14)

Of the wide range of setups, some showed no significant difference. The significant results are given in Table 1. The ID for the clean setup is a number to keep track of the different setups. The last column shows the difference between the PWL of the evaluation point in the real source map and the simulated source map. The best regression fit seems to follow from a line of independent point sources on the LE corner source with length 6-8 cm. The regression fits from best setups, ID 65, 66, 67, 68, 69 and 70, were also simulated on other frequencies. Source maps of the simulated regression fits for these six setups are shown in Figure 15, 16 and 17. The deviation of the evaluation points can be

found in Table 2. It is clear that these setups of source distributions have accurate fits. The source maps of the simulation are similar to the real source maps with the exception for some noise coming from other source as tunnel background noise, which is successfully ignored in the fit.

The regression fit can be used to calculate a value for the trailing edge noise. Noise spectra for the TE noise from setups 65, 66, 67, 68, 69, 70 and 28 (which is the first discussed setup with the assumption of single points sources on the corners) are given in Figure 18 and the difference with configuration 65 is displayed in Figure 19. It is observed that the different setups in processing the data do not heavily change the TE noise estimations above 1000 Hz. The setup where single point corner sources are assumed, differs the most but also that estimation is quite close to the others. Hence it can be concluded that the making of a regression fit is a robust method, which already comes quite close to the real source distribution.

To make a choice which setup will be used in the rest of the process, not only the deviations from Table 2 have been studied but also the source maps are compared. Based on the numbers of a single point and the visual data the choice is made to use setup 65 for the rest of the research.

ID Clean Setup	Leading Edge Corner (cm)	Trailing Edge Corner (cm)	Fit Points	PWL (dB)	Difference (dB)
43	3	3	Lines	50.577	0.499
44	4	3	Lines	50.536	0.458
47	3	3	Rectangle	50.636	0.558
48	4	3	Rectangle	50.548	0.47
51	2	3	Lines	50.609	0.531
52	2	3	Rectangle	50.718	0.64
53	1	3	Lines	50.633	0.555
54	1	3	Rectangle	50.783	0.705
61	5	4	Lines	50.477	0.399
62	5	4	Rectangle	50.444	0.366
65	6	4	Lines	50.446	0.368
66	6	4	Rectangle	50.369	0.291
67	7	4	Lines	50.439	0.361
68	7	4	Rectangle	50.365	0.287
69	8	4	Lines	50.411	0.333
70	8	4	Rectangle	50.368	0.29
71	9	4	Lines	47.072	3.006
72	9	4	Rectangle	43.476	6.602
73	10	4	Lines	41.867	8.211
74	10	4	Rectangle	43.54	6.538

Table 1- Power levels of evaluation point from the setups tested

ID Clean Setup	1000 Hz	1475 Hz	2500 Hz	Average
65	0.025	0.368	0.116	0.170
66	0.063	0.291	0.117	0.157
67	0.208	0.361	0.117	0.229
68	0.252	0.287	0.118	0.219
69	0.387	0.333	0.119	0.280
70	0.435	0.29	0.12	0.282

Table 2 - Difference of evaluation point power levels between real source map and simulated regression fit source map

4.1.2 Microphone setup

When looking at the placement of the microphones, (see Figure 20) some of the microphones are placed above and below the end plates of the test section. As a consequence, these microphones may not be able to measure the noise in the corners properly. Since corrections for microphone density and aperture are applied, the microphones at the outer circle are weighted more than the inner microphones. This could cause disturbance in the results when the outer microphones do not obtain good signals but are weighted more. However, adapting the weighting factors will decrease the resolution for beamforming which could decrease the quality of the results.

Regression fits have been obtained from the test case using different weighting factors for the microphones. In the first case the normal weighting factors are used which are used to correct for microphone density putting more weight on the outer circle of microphones. In the second case all microphones are equally weighted and in the third case the weighting factors from the first case are inverted putting more weight on the inner microphones.

Figure 21 shows the real source map and the simulated source maps obtained from the regression fits for the different microphone configurations. The simulations have a similar resolution since the simulation uses the same settings for every input. The case where equally weighted microphones are used, results in almost the same source map as the case where normally weighted microphones are used. The case where the weighting factors are inverted results in a different source map. The spurious noise sources are estimated higher especially for 2500 kHz.

Putting more weight on the inner microphones seems to deteriorate the results. Therefore, the normally used weighting will be used for further processing.

4.1.3 CLEAN step

When the regression fit works optimal the CLEAN step (see section 2.4) can be applied to refine the results. Figure 22 shows the clean source map obtained from the test case. The result is not in the form as expected like the simulations showing a clean representation of the TE noise. Instead, all the noise seems to switch halves and at some points a strong unrealistic high point source is displayed. Multiple cases and setups show similar results which is not usable to evaluate TE noise.

Figure 23 displays the output obtained from the test case. The regression fit shows in the middle a perfect equally distributed line of sources at the TE as was imposed. However, the clean output has divided the sources into higher and lower values. Even NaN outputs are given which probably means that the sound power is negative. This is not physical but to compensate for this negative power, some other sources have rather high power levels. This is what likely causes the high level points in the source maps.

Apparently the deconvolution steps do not properly remove the source contribution. Therefore, it is possible that a source point is underestimated or ignored which results into low, zero or even negative values. When that happens probably the next source is overestimated to compensate. This process gives invalid results which cannot be used for the evaluation of TE noise. One possible solution might be basing the deconvolution solely on the CSM instead of the auto powers. This could overcome the errors introduced by the PSF. However, this is outside the scope of this research and will not be investigated further.

Though the result obtained with deconvolution is not usable, the source distribution based on the regression fit seems to be accurate. Therefore, the results from the regression fit will now be used only to evaluate TE noise and the other sources.

4.2 Source Decomposition

The source distribution concerns not only the TE but also all the other spurious sources. Therefore, the source strengths of the spurious sources are also known. It was assumed that there are in total four significant spurious noise sources: the LE upper corner source, the LE lower corner source, the TE upper corner source and the TE lower corner source. Figure 24 displays the spectra of all the sources.

The two LE corner sources do follow a similar trend. For the rest it is harder to find a trends but it is clearly visible that the noise originating from spurious sources is of considerable power level. Figure 25, 26, 27 and 28 show that the noise coming from spurious sources is even larger than the TE noise in the lower frequency domain below 4000 Hz for different cases. This means that the algorithm can be of significant value for the TE measurements in the lower frequency domain.

One way to evaluate whether the spurious noise sources are filtered out is to study the behavior. For example, noise originating from the LE should be independent of the configuration mounted on the TE. Figure 29 and 30 show the LE noise from the upper and lower corner. The sound powers for different configurations are approximately of similar strength and are almost overlapping with the exception of some difference in the high frequency range. This proves that indeed the LE corner sources are independent form TE noise. From this, it can be concluded that the LE corner sources are filtered out properly and do not influence the TE noise estimation. Providing similar conclusions for the TE corners is more difficult because these sources are influenced by the serrations mounted on the TE. However, the correct behavior of the LE sources, plus the accuracy of the regression fit, is already an indication of a well performing algorithm.

4.3 Scaling

To compare results, scaling rules can be applied. For the case of comparing TE noise for different velocities an often used scaling rule is :

$$PWL_{norm} = PWL_{n1/3} - \log_{10}(U^5 \delta^*) \quad (30)$$

for the sound power and

$$St_{\delta^*} = \frac{f \delta^*}{U} \quad (31)$$

for the frequency. With $PWL_{n1/3}$ is meant the third octave band power level normalized on bandwidth:

$$PWL_{n1/3}(f) = \frac{PWL_{1/3}(f)}{bw(f)} \quad (32)$$

δ^* is the so called displacement thickness which is a measure for the boundary layer thickness. This number can be obtained from experiments and Xfoil simulations of the previous experiment. Figure 31 displays the TE noise calculated from a BPM model of a NACA 0012 airfoil. The graphs display the TE noise originating from the suction side and the pressure side. Table 3 provides the displacement thickness for both the NACA 0012 and DU-96-W-180 for the suction and the pressure side. Because the NACA 0012 airfoil is symmetric, the displacement thickness and the noise levels are equal for 0 AoA. But at a higher AoA, the displacement is thicker on the suction side than on the pressure side. From the figures, it can be seen that at higher AoA the noise peaks shift from each other and that the noise

originating from the suction side becomes the dominant. A thicker displacement results in higher noise level at lower frequency.

AoA _{eff}	0	6	8.2
$\delta_{s,NACA}^*$ (cm)	0.6442	1.646	3.409
$\delta_{s,DU}^*$ (cm)	1.4	2.4	3.3
$\delta_{p,NACA}^*$ (cm)	0.6442	0.390	0.339
$\delta_{p,DU}^*$ (cm)	0.60	0.34	0.27

Table 3 - Displacement thickness for BPM of NACA 0012 and for Xfoil simulation of DU-96-W-180 at 70 m/s

The same behaviour for the displacement thickness can be observed for the DU-96-W-180 airfoil and because the airfoil is not symmetric, the difference is even larger. Hence of the DU-96-W-180 airfoil can be said that for positive AoA, the dominant part of the TE noise is originating from the suction side. For this reason, the displacement thickness of the suction side is used for scaling.

Figure 32 and 33 display the velocity scaled noise levels for different cases. Third order polynomial fits have been used to represent a trend in the data. The noise levels do not collapse entirely. The noise levels for the higher velocity seem to be consequently too low or too much shifted to the left. Table 4 shows the total decibel level for the velocity scaled data from different cases. The sixth column shows the standard deviation for the different velocities. For most cases the deviation is within 1 dB which is quite good for a scaling. This gives rise to the idea that the scaling on power level is correct but the scaling on frequency should be chosen different.

Velocity	70	60	50	40	std
Clean 0 AoA	-11.193	-10.354	-9.5253	-9.1167	0.92108
Clean 10.51 AoA	-10.8	-10.249	-9.4394	-8.7545	0.89901
Clean 14.37 AoA	-11.064	-10.634	-9.6501	-7.972	1.3729
US-TOP 0 AoA	-11.305	-11.221	-10.952	n.v.t.	0.18459
US-TOP 10.51 AoA	-13.274	-13.009	-12.798	n.v.t.	0.23869
US-TOP 14.37 AoA	-14.732	-14.438	-14.066	-14.791	0.33208
FS 0 AoA	-16.229	-16.368	-16.072	-15.561	0.35231
FS 10.51 AoA	-15.881	-16.07	-16.739	-16.203	0.36844
FS 14.37 AoA	-16.841	-17.541	-17.347	-17.042	0.31174
US-BOT 0 AoA	-8.6124	-8.0458	-7.723	-7.6927	0.42697
US-BOT 10.51 AoA	-11.486	-11.539	-11.531	-11.727	0.10684
US-BOT 14.37 AoA	-13.871	-13.828	-14.339	-15.359	0.71196

Table 4 – Total power level for the velocity scaled data (U^5)

Brooks mentioned that there is a relation between peak location and velocity:

$$St_{peak} = 0.02M^{-0.6} \sim U^{-0.6} \quad (33)$$

Data from other sources also support this idea that noise spectra shift according to the above relation. This means that the frequency should be scaled according to:

$$\frac{St_{\delta^*}}{St_{peak}} \sim \frac{f\delta^*}{U^{0.4}} \quad (34)$$

Figure 34 and 35 show the power level plots with the upper mentioned scaling used. These power levels already show a better data collapse. Another empirical based scaling rule is to scale the power level with $U^{4.5}$. Plots of these scaled power levels are given in Figure 36 and 37. This type of scaling shows better data collapse than Brooks scaling. When looking at Table 5, the deviation of the total scaled power deviates also only within 1 dB. Hence scaling on $U^{4.5}$ is also a good scaling rule.

Concluding, both scaling on U^5 and $U^{4.5}$ give good data collapses. This is proof for good quality of the results. The scaling on the frequency range could be optimized to obtain a better collapse. However, the peak relation from Brooks already gives a good data collapse on the results which confirms the statement that the results are valid.

Velocity	70	60	50	40	std
Clean 0 AoA	-1.9674	-1.4635	-1.0305	-1.1064	0.42759
Clean 10.51 AoA	-1.5749	-1.3578	-0.94454	-0.7442	0.37882
Clean 14.37 AoA	-1.839	-1.7432	-1.1552	0.038269	0.86337
US-TOP 0 AoA	-2.0798	-2.3304	-2.457	n.v.t.	0.19199
US-TOP 10.51 AoA	-4.049	-4.1187	-4.3033	n.v.t.	0.1314
US-TOP 14.37 AoA	-5.5067	-5.547	-5.571	-6.7808	0.62019
FS 0 AoA	-7.0031	-7.4771	-7.5772	-7.5506	0.26931
FS 10.51 AoA	-6.6555	-7.1789	-8.2443	-8.1924	0.78127
FS 14.37 AoA	-7.6155	-8.6502	-8.8526	-9.032	0.63417
US-BOT 0 AoA	0.61313	0.845	0.77187	0.31765	0.23382
US-BOT 10.51 AoA	-2.2609	-2.6479	-3.0357	-3.7169	0.62098
US-BOT 14.37 AoA	-4.6453	-4.9372	-5.8444	-7.3488	1.2157

Table 5 - Total power level for the velocity scaled data ($U^{4.5}$)

4.4 Comparison with old results

It is of interest what the difference in results are compared to the earlier way used to measure. In the previous conducted experiment, the middle point of the conventional source map was taken to evaluate the TE noise. Especially at low frequencies this point is heavily influenced by the spurious noise sources which are of considerable strength and the lack of resolution causing multiple sources to have a heavier overlap at low frequencies. Therefore, the TE noise is probably overestimated for lower frequencies. For higher frequencies the trend should be somewhat similar.

To compare spectral shapes, the old spectra are off-set to match the new spectra at 6300 Hz. Figure 38 gives a plot of the TE noise obtained from old and new methods. In the lower frequencies the noise is much lower for the new method than for the old method. This is probably because of the overestimation in the old method. Hence the new method is better in determining TE noise spectra. Because of the lower power levels in the low frequency range it is now possible to recognize a peak in the data.

According to literature the frequency of the peak is inversely proportional to the displacement thickness. Therefore, this peak should shift to lower frequency for higher AoA. When looking at Table 3, one can see that the displacement thickness on the suction side doubles in size going from effective AoA 0 to 8.2 (14.37 geometric). This would mean that the peak frequency gets twice as small. Looking at Figure 38, this seems not to be entirely followed up due to

some high pitch noise for AoA 10.51 but for AoA 14.37 and AoA 0, two peaks can be recognized at 2000 Hz and 4000 Hz.

It seems that on lower frequencies the sound power level goes up again. Figure 39 shows the same new spectra but for a wider frequency range. The sound power level shows indeed higher values at frequency ranges below 1000 Hz. It is unsure what causes this noise. It could be another peak in TE noise since noise is radiated from both suction side and pressure side, but the frequencies are quite low and there does not seem to be a frequency shifting which is expected for TE noise. It is also possible that this is background noise but if that is the case, the algorithm should not be recognizing this as TE noise. In Tuinstra's paper, the results below 1000 Hz also became less accurate so the raising in noise levels is probably due to the inaccuracy of the algorithm (see also Figure 5). At lower frequencies TE noise is expected to be lower but the spurious noise sources stay of similar strength. As it gets harder to distinguish different noise sources at lower frequencies the algorithm might address higher values to the TE noise. Hence results below 1000 Hz should be neglected.

In short, compared to the old results, the extended CLEAN-SC algorithm results in probably more accurate lower power levels in the lower frequency range. Because of this it is possible to recognize peaks in the spectra. However, below 1000 Hz, the power level is quite high and it is probably caused by the inaccuracy of the algorithm. This should be investigated further.

4.5 Use of Serrations

Now that the extended CLEAN-SC algorithm is successfully applied, the results for different serrations could be revisited.

Figure 40 and 41 show the spectra for different serrations compared and Figure 42 and 43 show the noise reduction obtained compared to a clean TE.

From the plots it is concluded that the flexible serrations perform best at all AoA. Especially in the high frequency range the FS result in a large noise reduction. The US-TOP and US-BOT serrations only perform well at high AoA because they were designed to align with the flow at high AoA. At that point the US-TOP serrations have slight better performance.

In the old study averages were taken over all cases with a frequency range of 1250-8000 Hz. The FS performed the best with an average reduction of 4.6 dB with a best performing case with average reduction of 8.5 dB. The second best serrations, US-TOP had an average reduction of 2.6 dB and a best case of 5.4 dB. The third best serrations, US-BOT resulted in an average reduction of 1 dB over all cases.

According to the new results FS is still the best type of serrations with an average reduction over all cases of 5.1 dB over 1250 – 8000 Hz and even 5.6 dB over 1000-10000 Hz. However, the wider range is not comparable to the old case. A best case was found to reduce noise with 8 dB in the short range. The US-TOP configuration showed an average reduction of 2.4 dB and the US-BOT an average of 1.4 dB.

The conclusions drawn from the new algorithm are similar to the conclusions from the previous method. Still, the determined performance in noise reduction seems to be slight better. This could be because of the lower noise levels in TE noise obtained from the lower frequencies, emphasizing the more relevant higher frequencies.

5 Conclusions and Recommendations

The goal of this research was to evaluate an extension of the CLEAN-SC algorithm, applied to TE noise. The Algorithm consisted of two steps. The first deconvolution step by linear regression based on theoretical PSF and a second iterative deconvolution based on empirical PSF. It was found that the first step yields robust results. The second step can provide non-physical results and was found less robust.

The spurious corner sources exhibit high levels, often exceeding that of the TE sound power.

Scaling rules were applied on the TE noise data which resulted in a good data collapse, which confirmed that the obtained TE noise results behave as expected according to literature.

The algorithm was able to separate the noise from other sources for frequencies above 1 kHz. Below this value the resolving power was not sufficient.

The conclusions on the use of serrations for the experiment have been confirmed by the results coming from the new algorithm. The serrations show an even better performance. The best type of serrations namely the flexible serrations, cause an average noise reduction of 5.1 dB compared to 4.6 dB according to the old method.

6 Figures

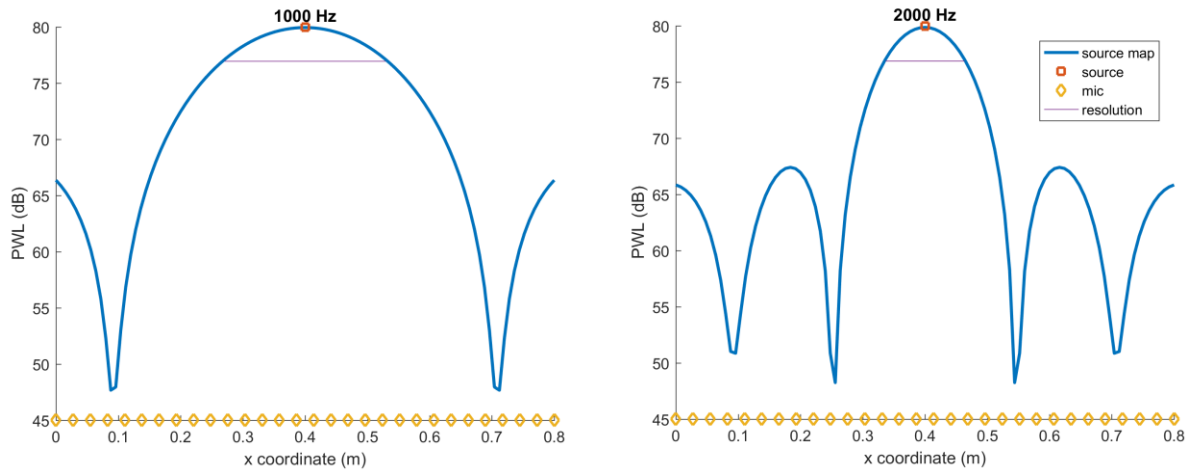


Figure 1 - 2D source map of a single simulated source of 1000 Hz (left) and 2000 Hz (right)

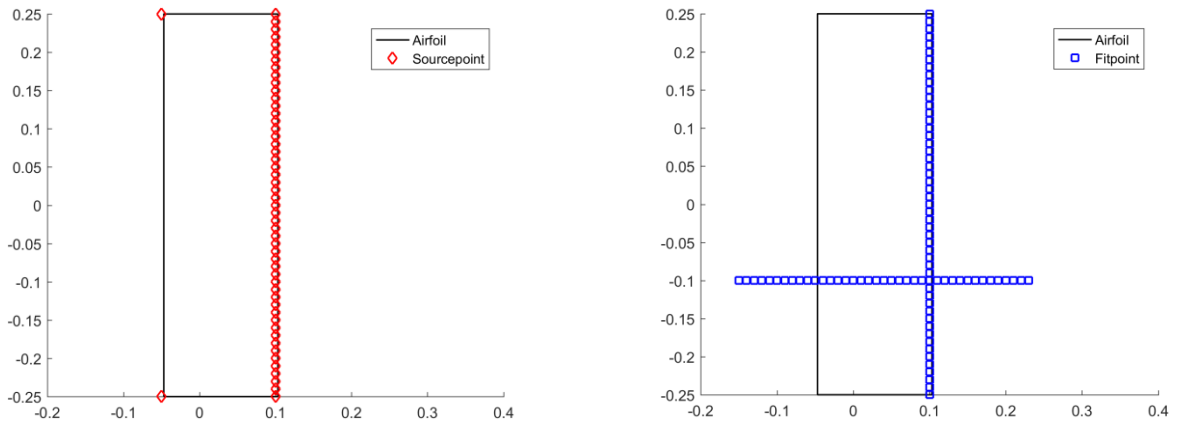


Figure 2 - Simulated source points (left) and fit points used for regression fit (right)

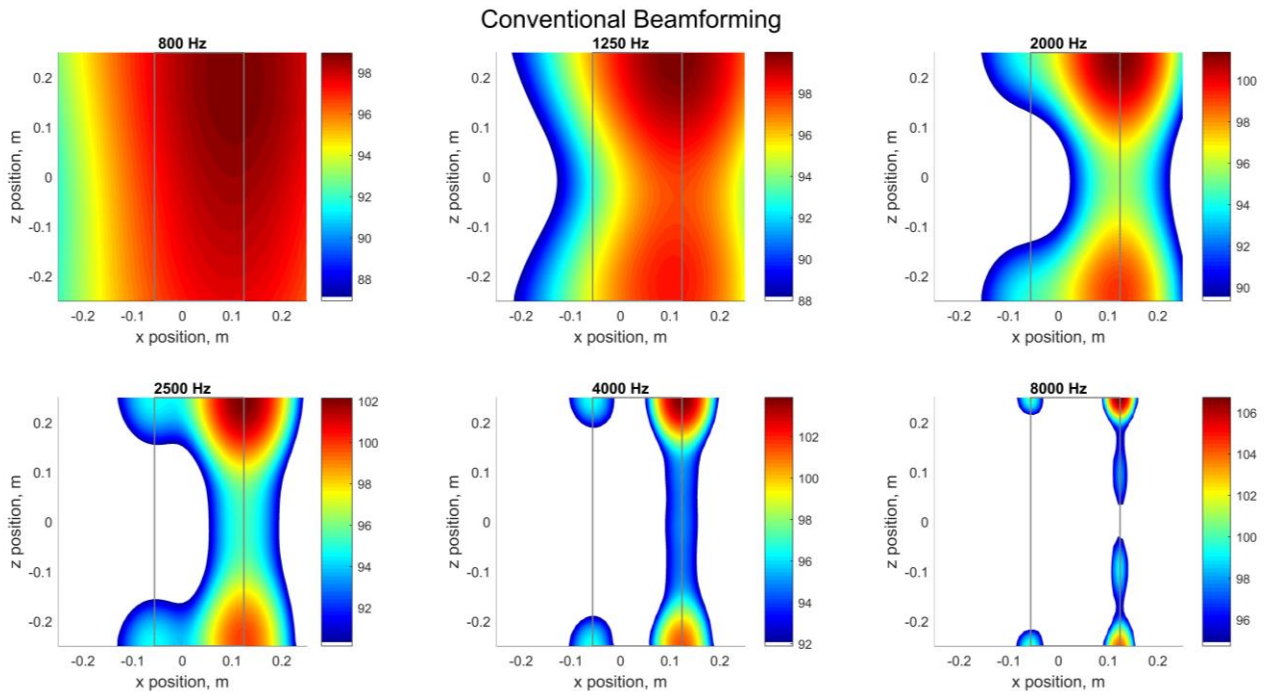


Figure 3 - Source maps of simulated sources obtained with Conventional Beamforming

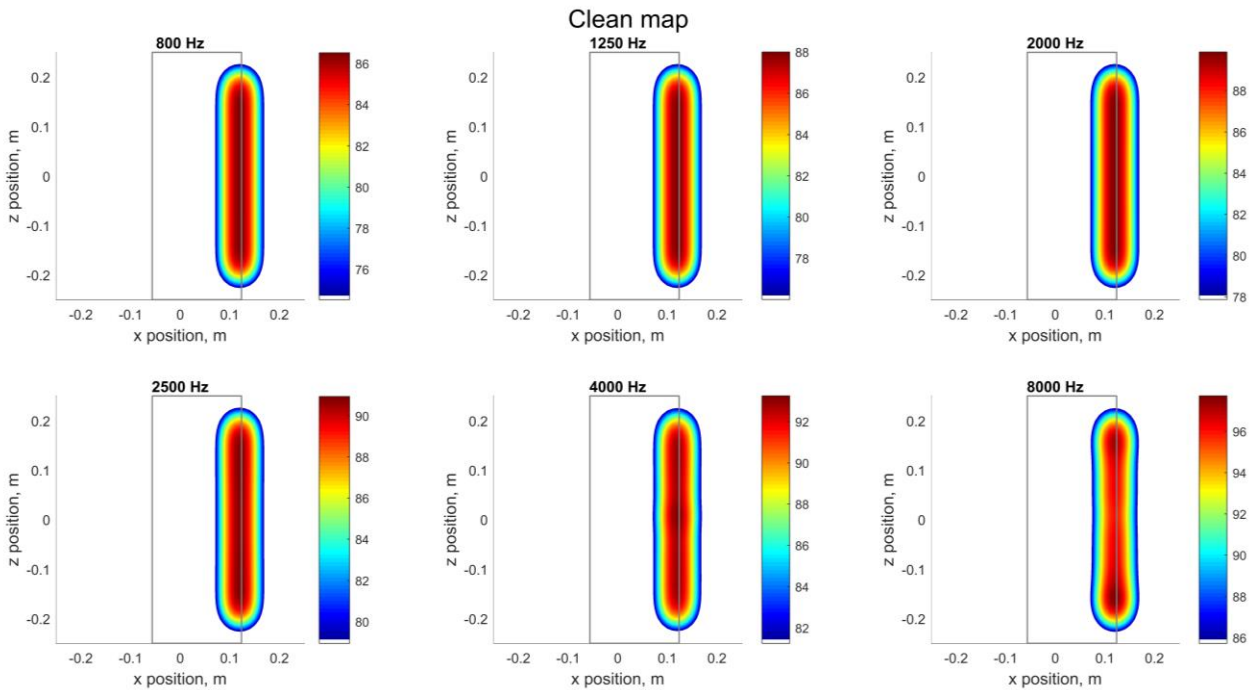


Figure 4 - Source maps of simulated sources obtained with the extension on the CLEAN-SC algorithm

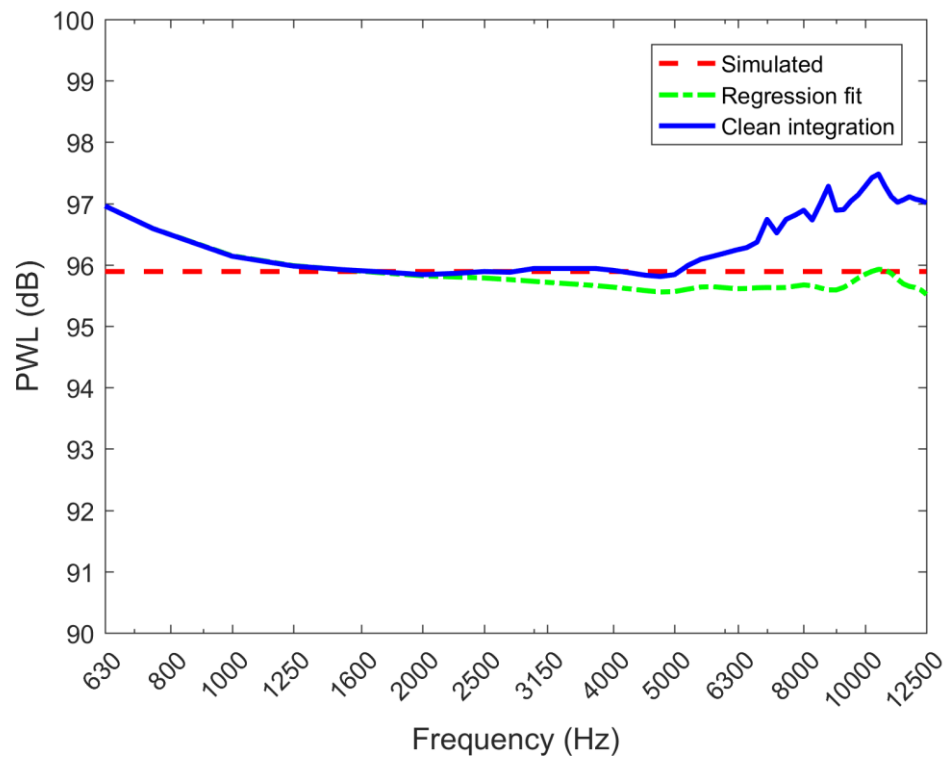


Figure 5 - Power spectrum of the simulated TE noise

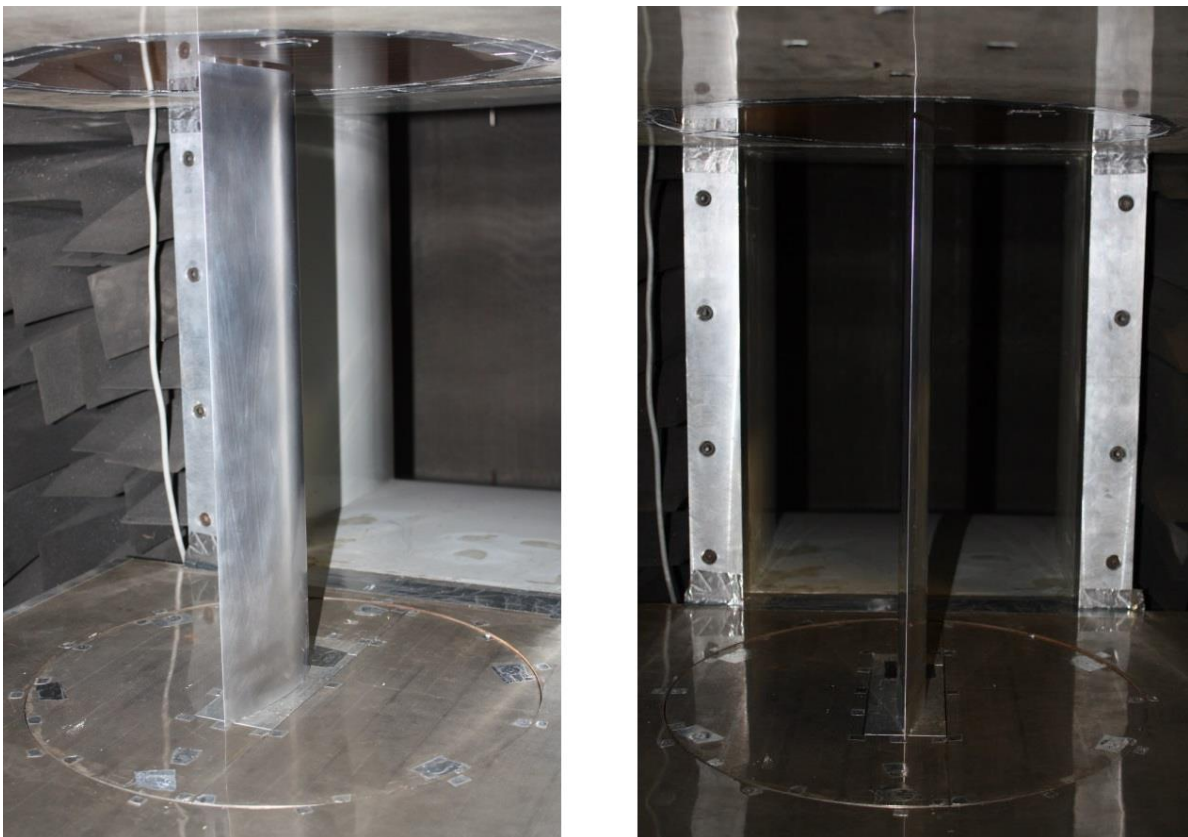


Figure 6 - DU-96-W-180 Airfoil, spanned between the end plates on the rotating balance, which sets different AoA automatically. The 0.38×0.51 m nozzle is shown behind the airfoil.

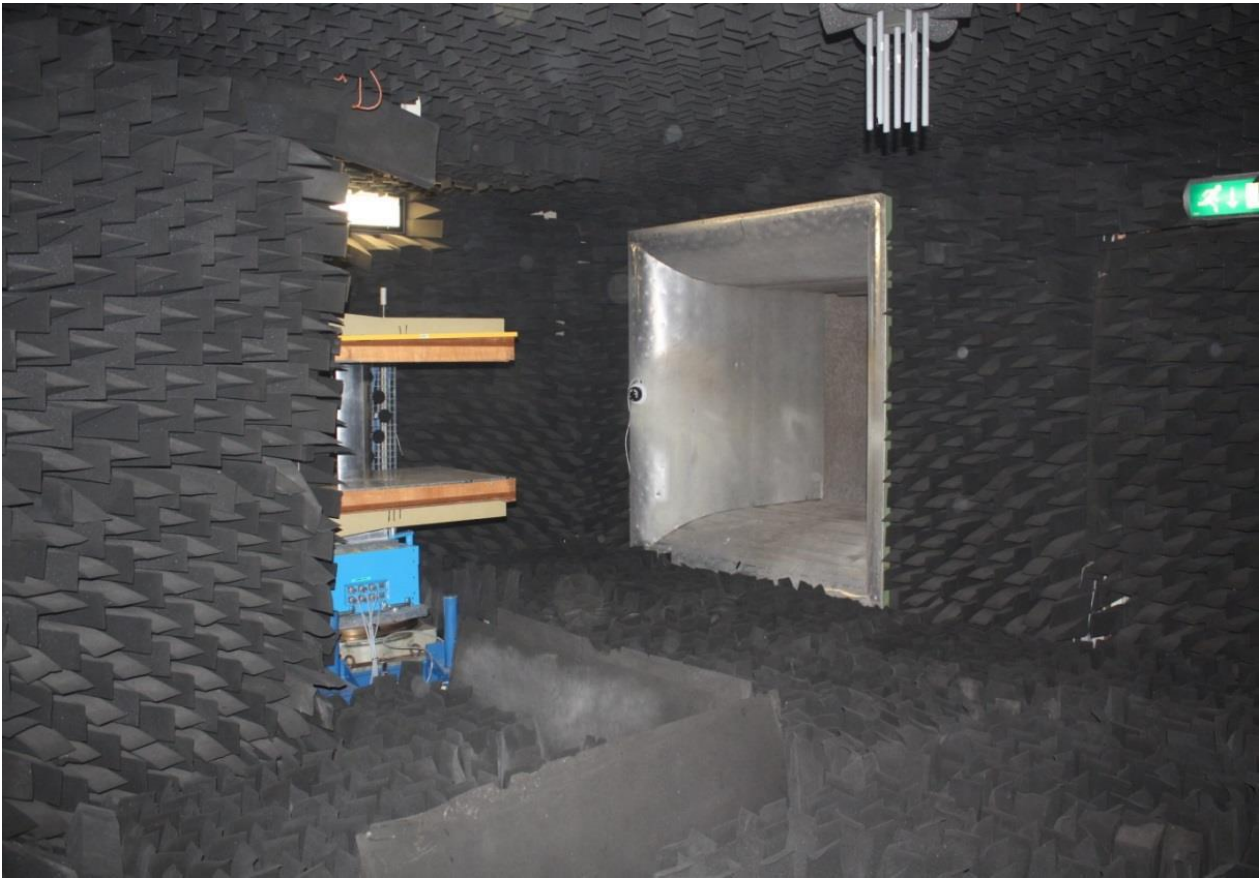


Figure 7 - Anechoic room with 0.5 m foam wedges

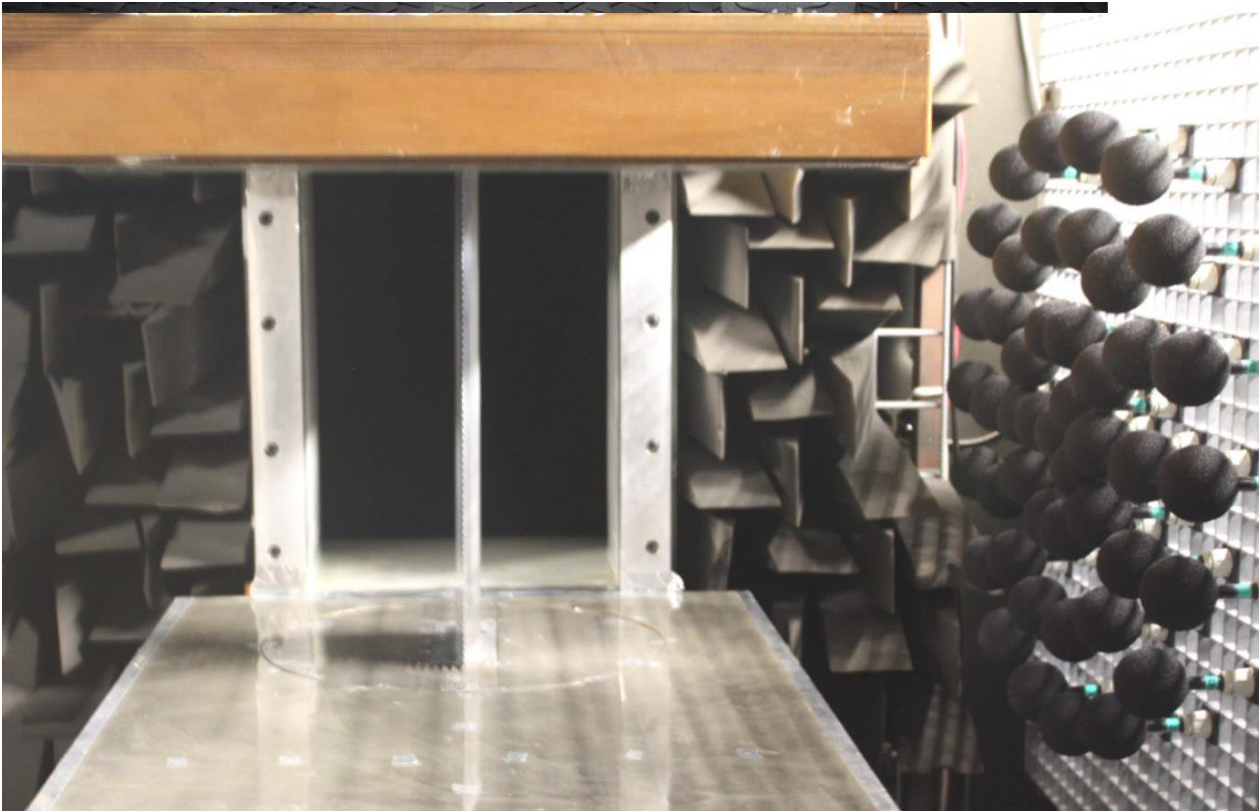


Figure 8 - Microphone array on the suction side of the airfoil (0.6 m from the tunnel axis)

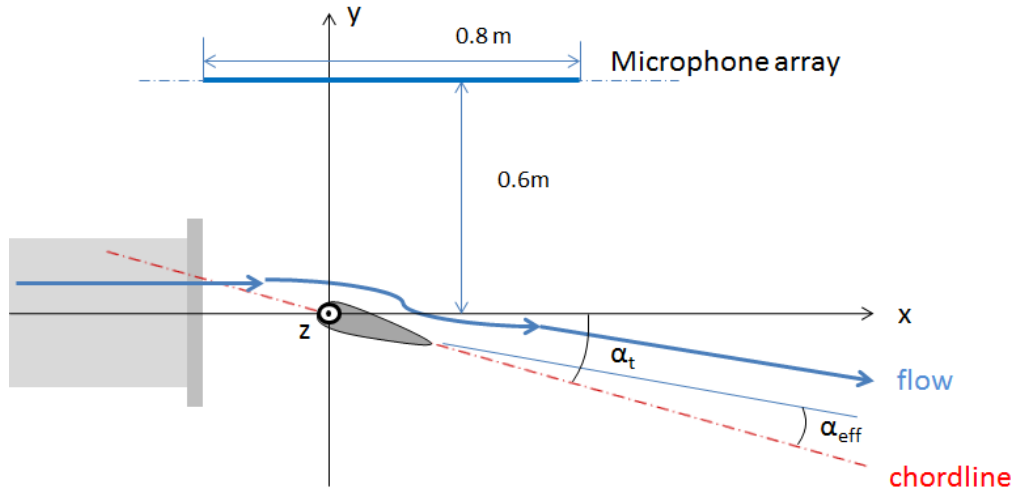
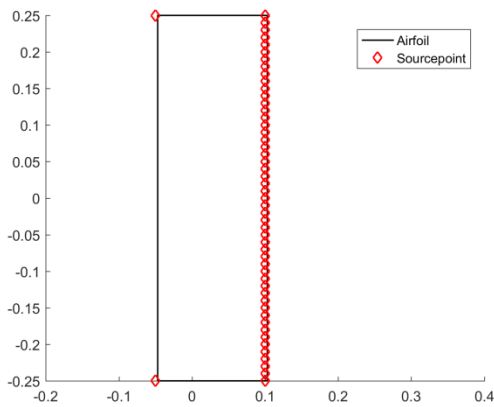
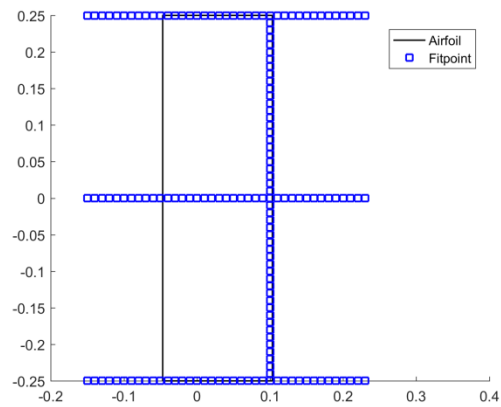


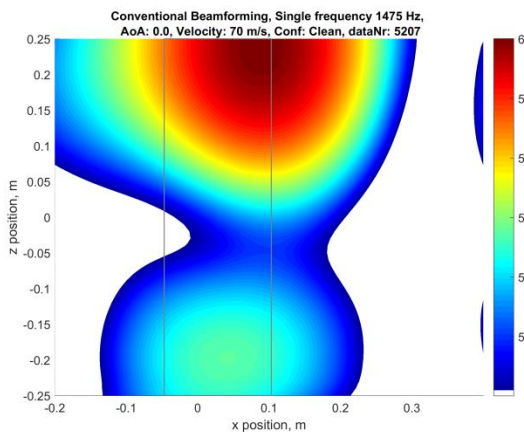
Figure 9 - Coordinate system for acoustic measurements



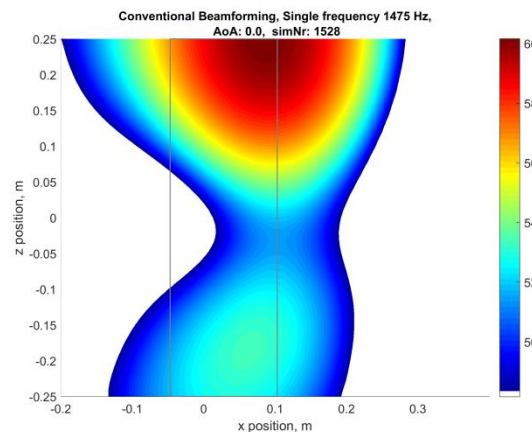
a)



b)



c)



d)

Figure 10 - Assumed source points (a), fit points (b), measured source map (c) and simulated source map (d) at 1475 Hz of case with clean configuration 0 AoA and 70 m/s

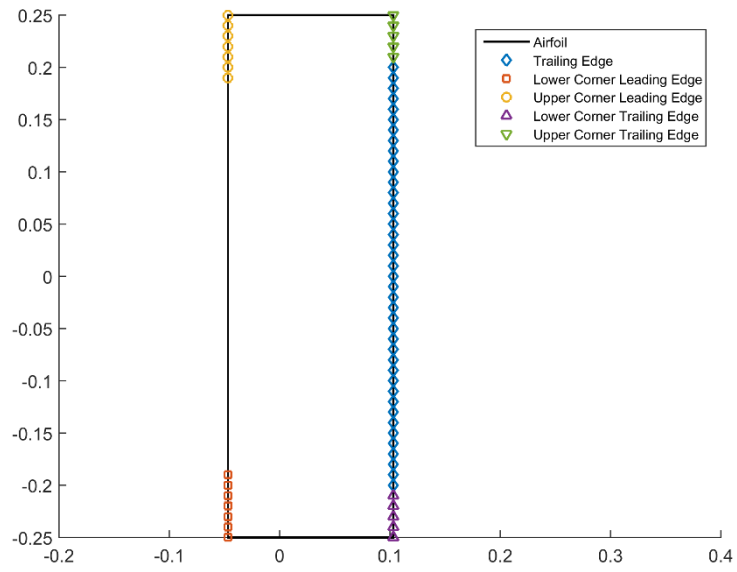


Figure 11 - Assumed source distribution with line sources along LE corners

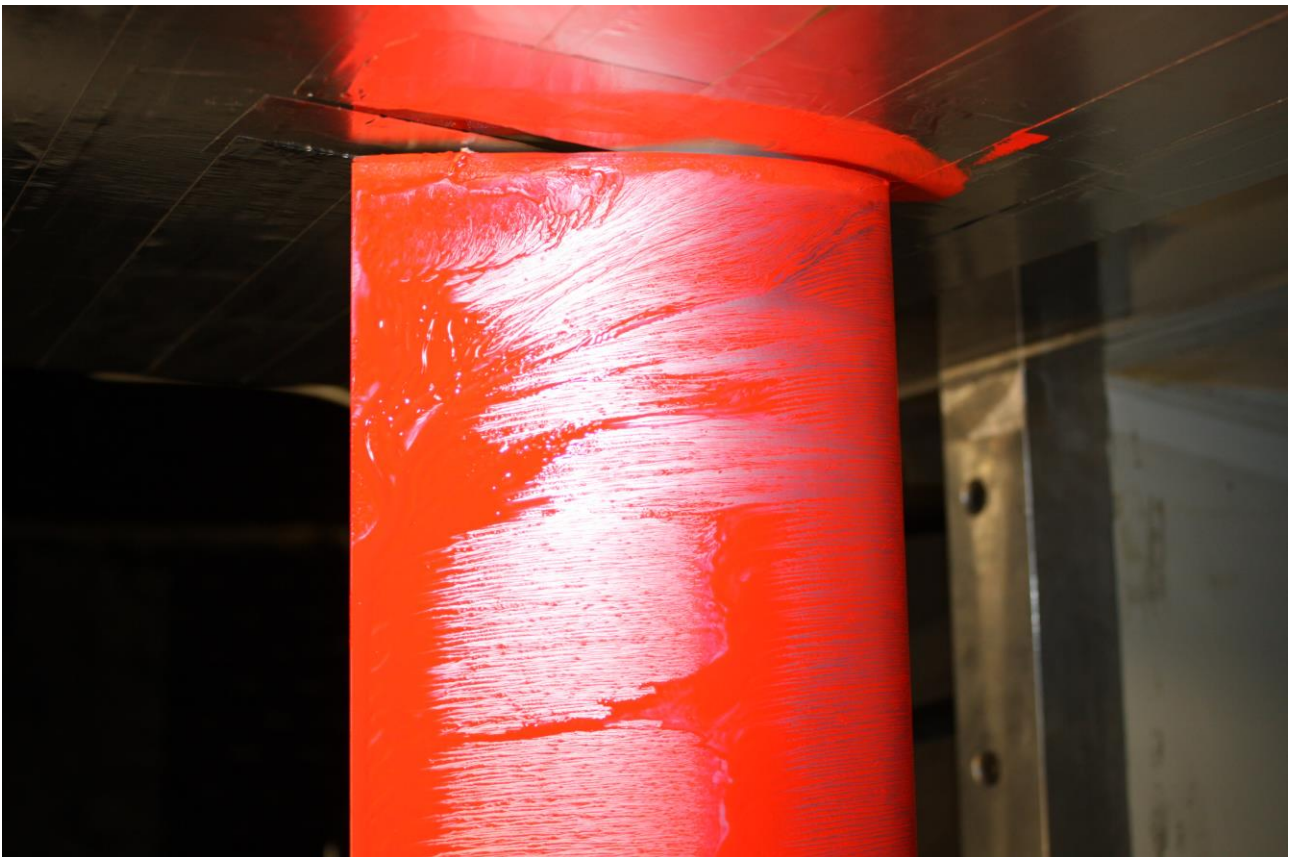


Figure 12- Visualization of the flow near the end plate

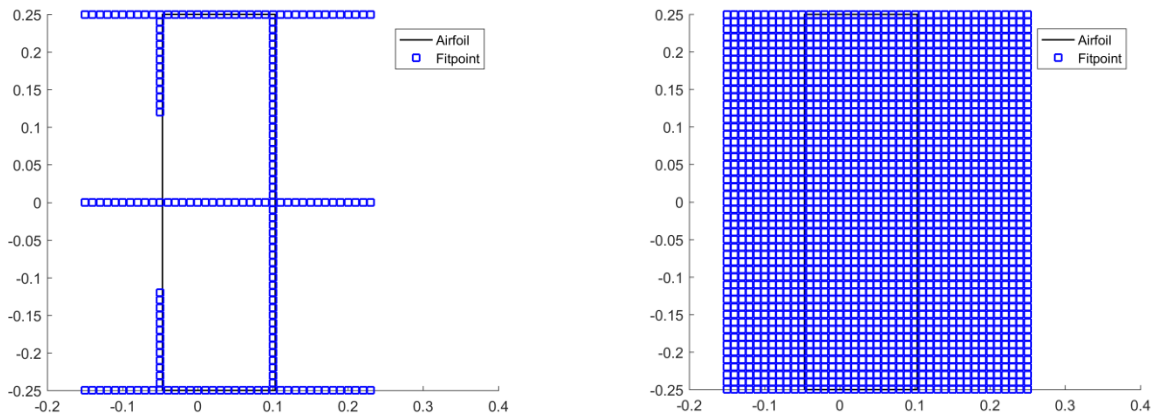


Figure 13 - Set of fit points using lines (left) and all the points within a rectangle (right)

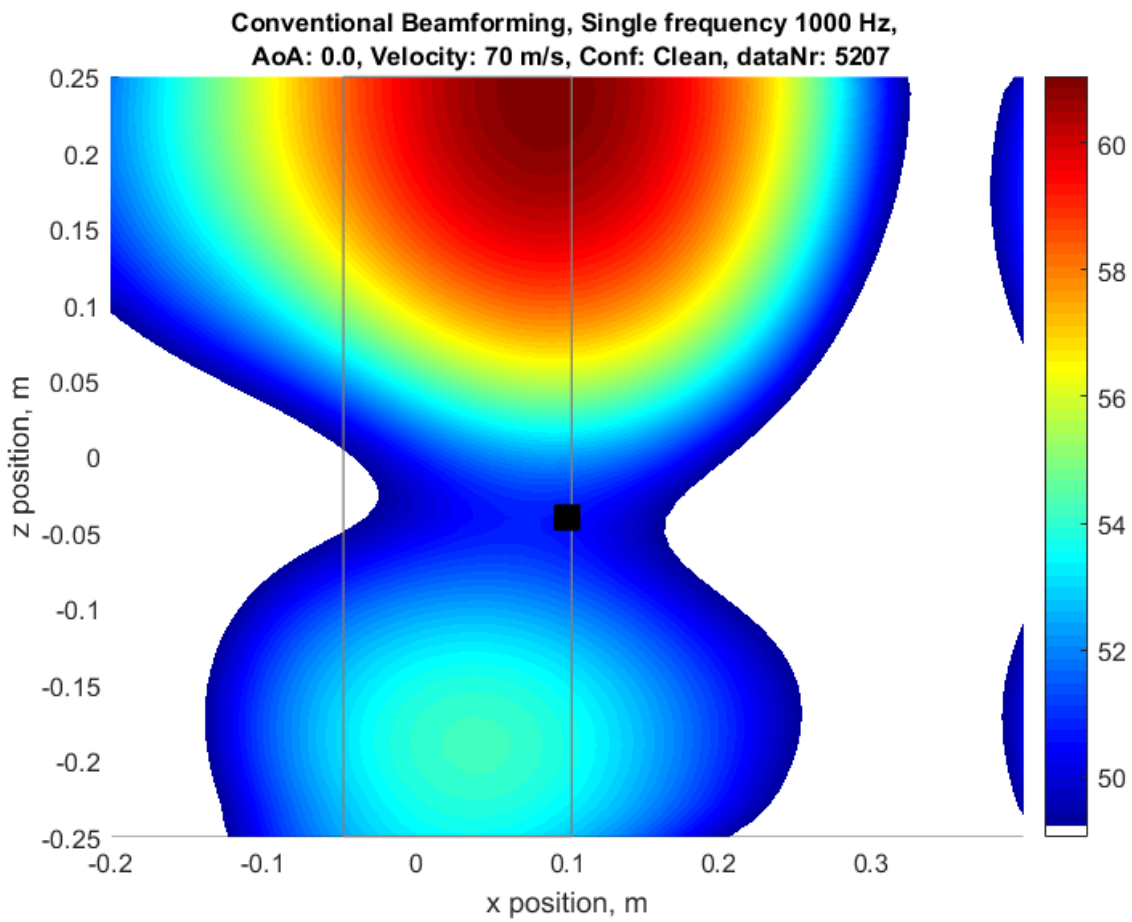
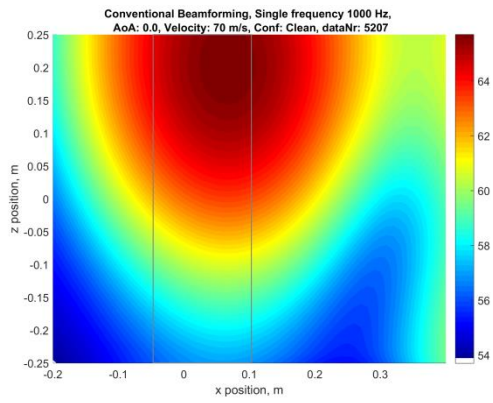
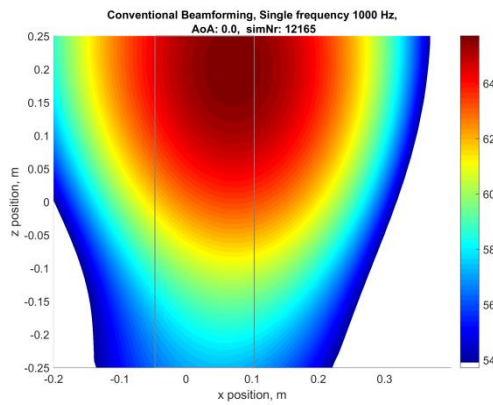


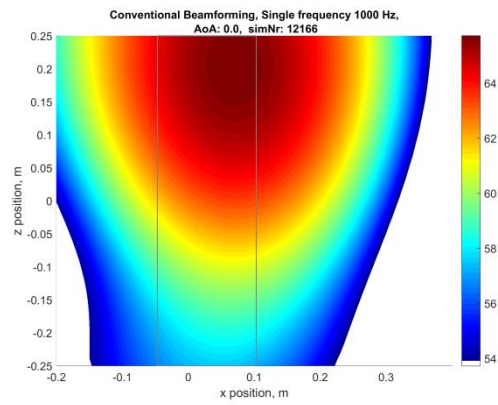
Figure 14 - Source map on the test case with a black dot to represent the evaluation point



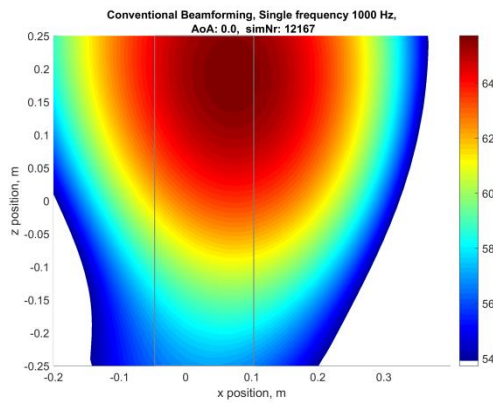
a)



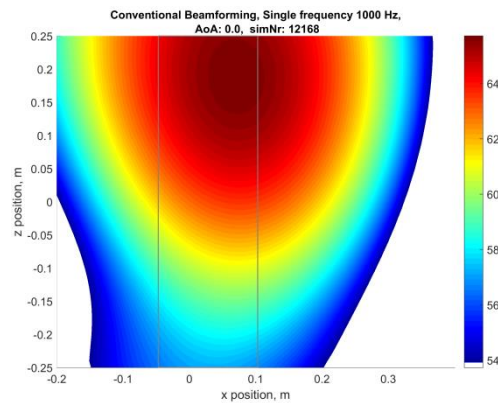
b)



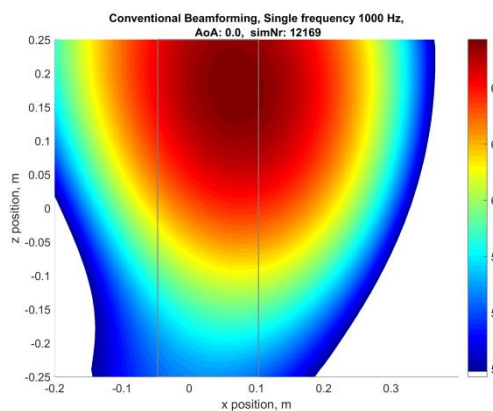
c)



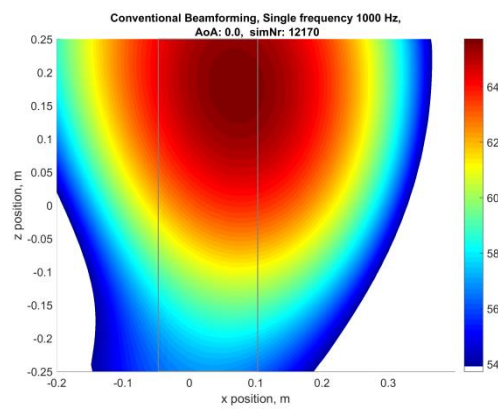
d)



e)

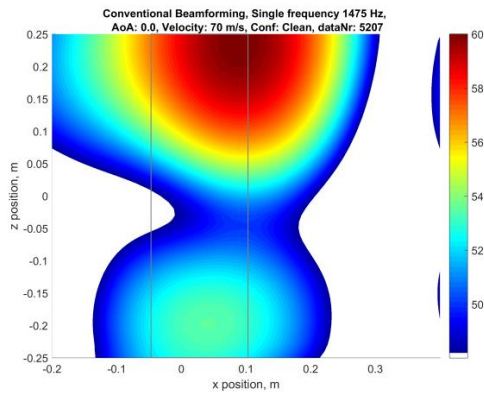


f)

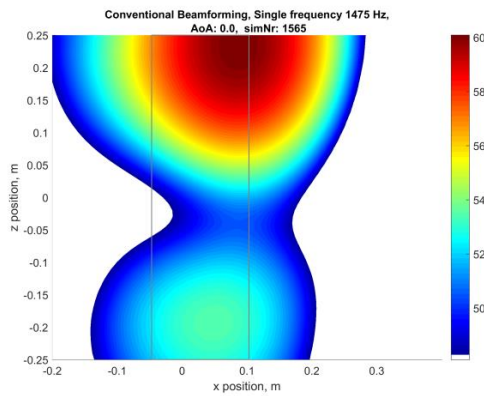


g)

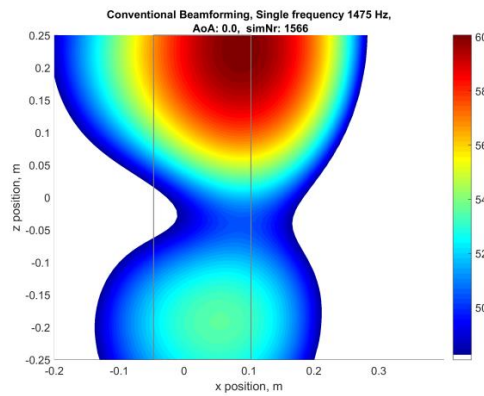
Figure 15 - Source maps of real case (a) and simulated regression fits from setup 65 t/m 70 (b t/m g) respectively at 1000 Hz



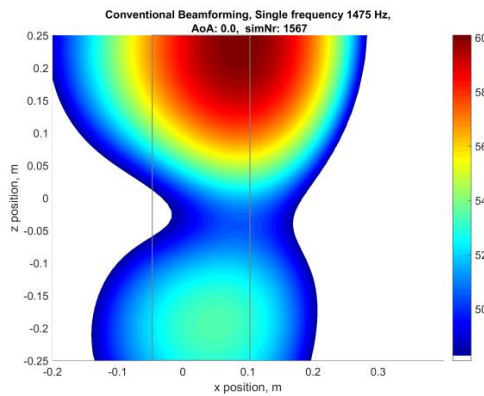
a)



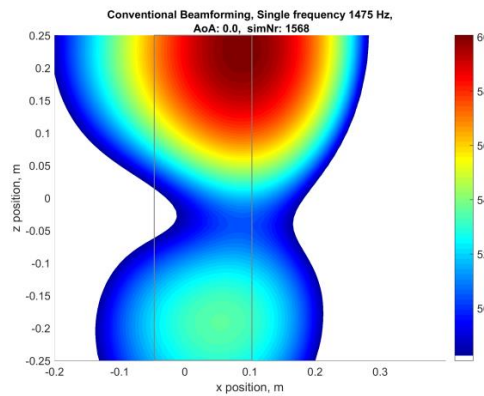
b)



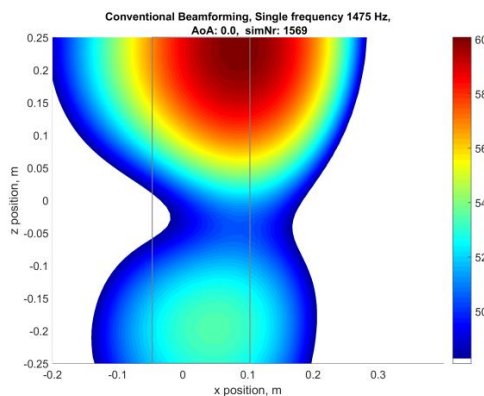
c)



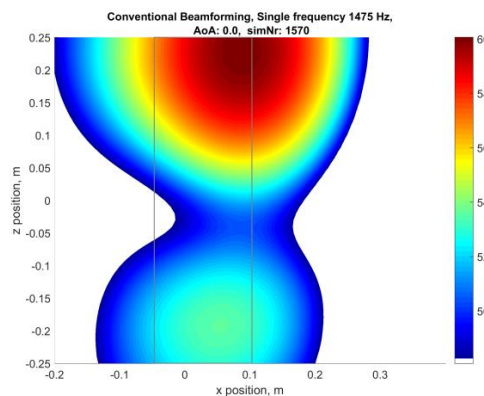
d)



e)



f)



g)

Figure 16 - Source maps of real case (a) and simulated regression fits from setup 65 t/m 70 (b t/m g) respectively at 1475 Hz

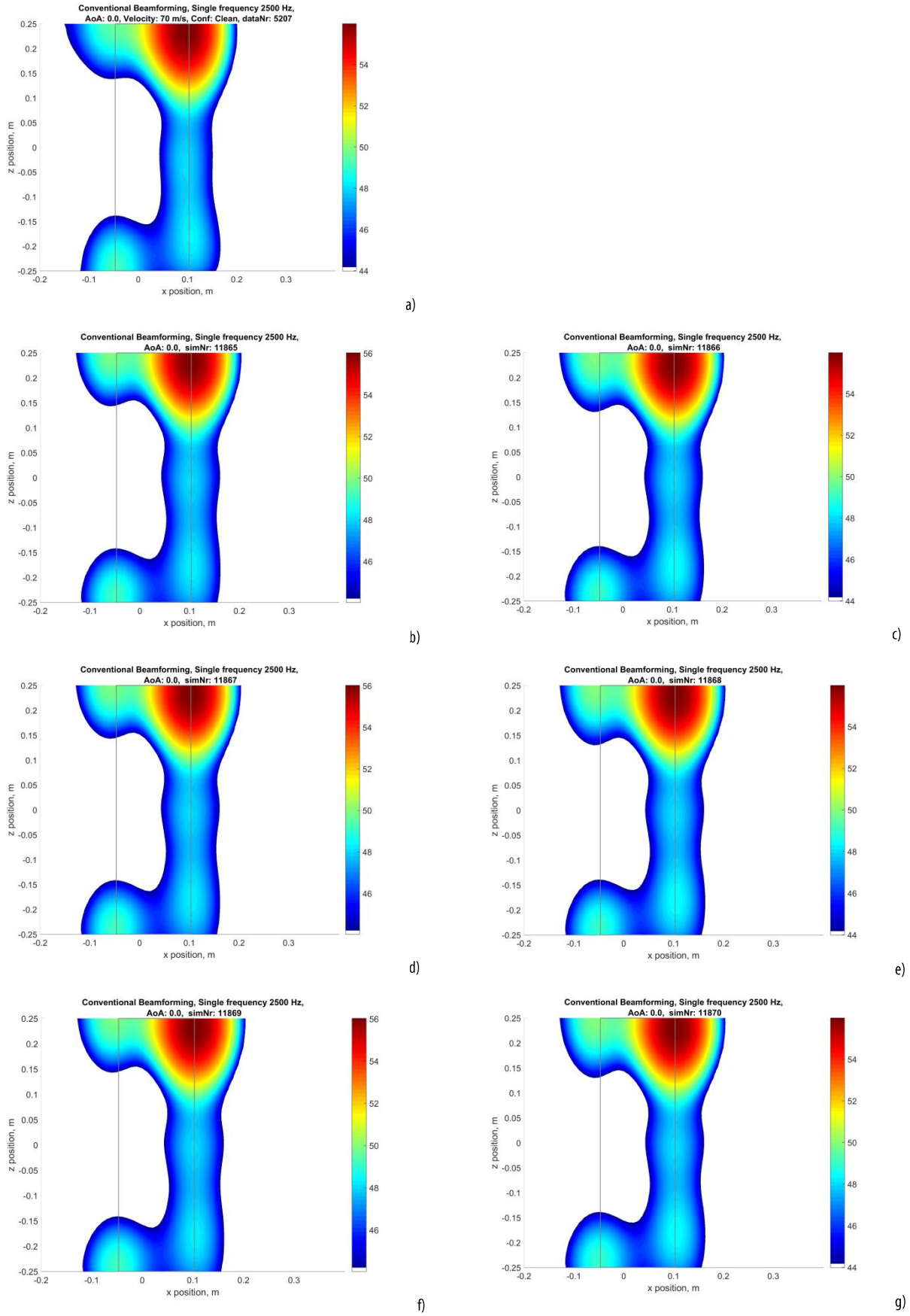


Figure 17 - Source maps of real case (a) and simulated regression fits from setup 65 t/m 70 (b t/m g) respectively at 2500 Hz

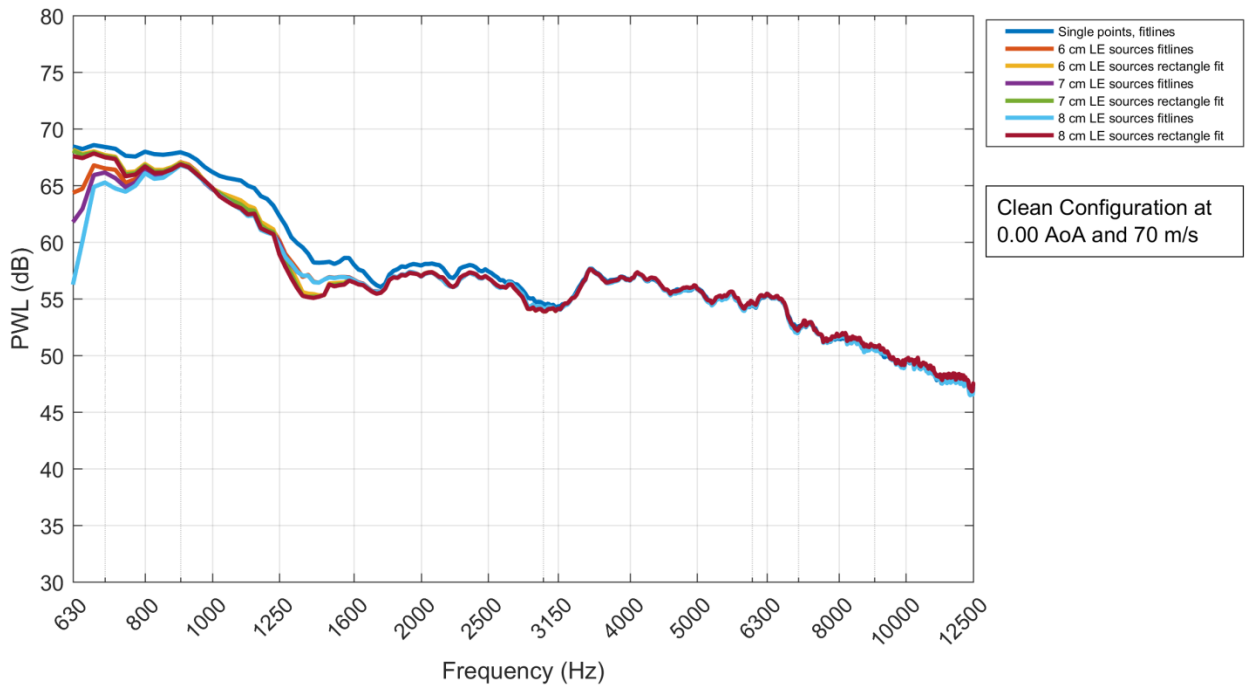


Figure 18 – Narrowband noise spectra of TE noise calculated from regression fit for setups 28, 65, 66, 67, 68, 69 and 70

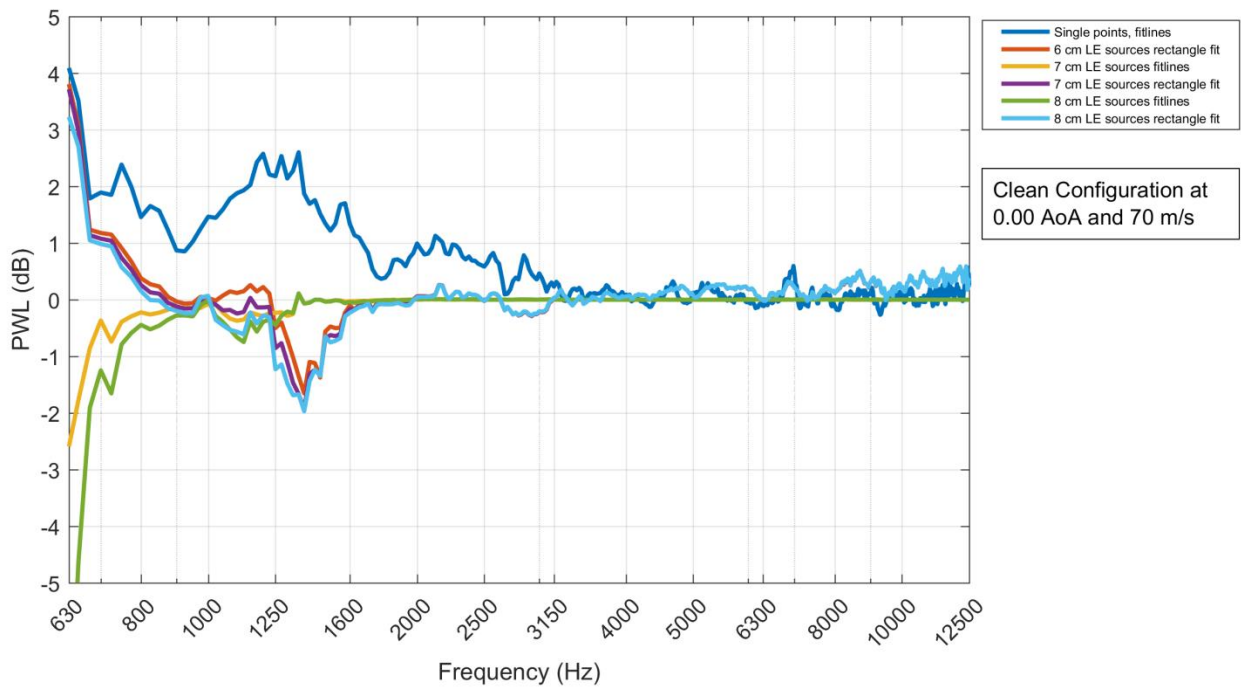


Figure 19 - Difference in narrowband noise spectra of TE noise calculated from regression fit for setups 28, 66, 67, 68, 69 and 70 compared with 65

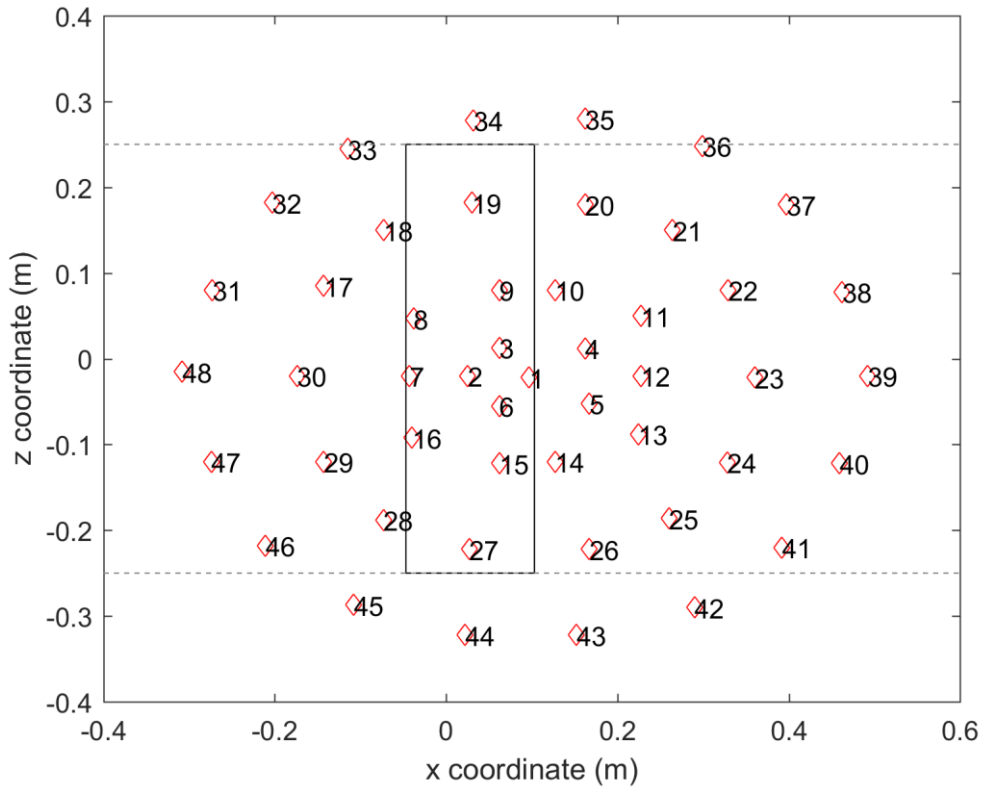


Figure 20 - Location of each microphone, airfoil and endplates (dashed line) visualized

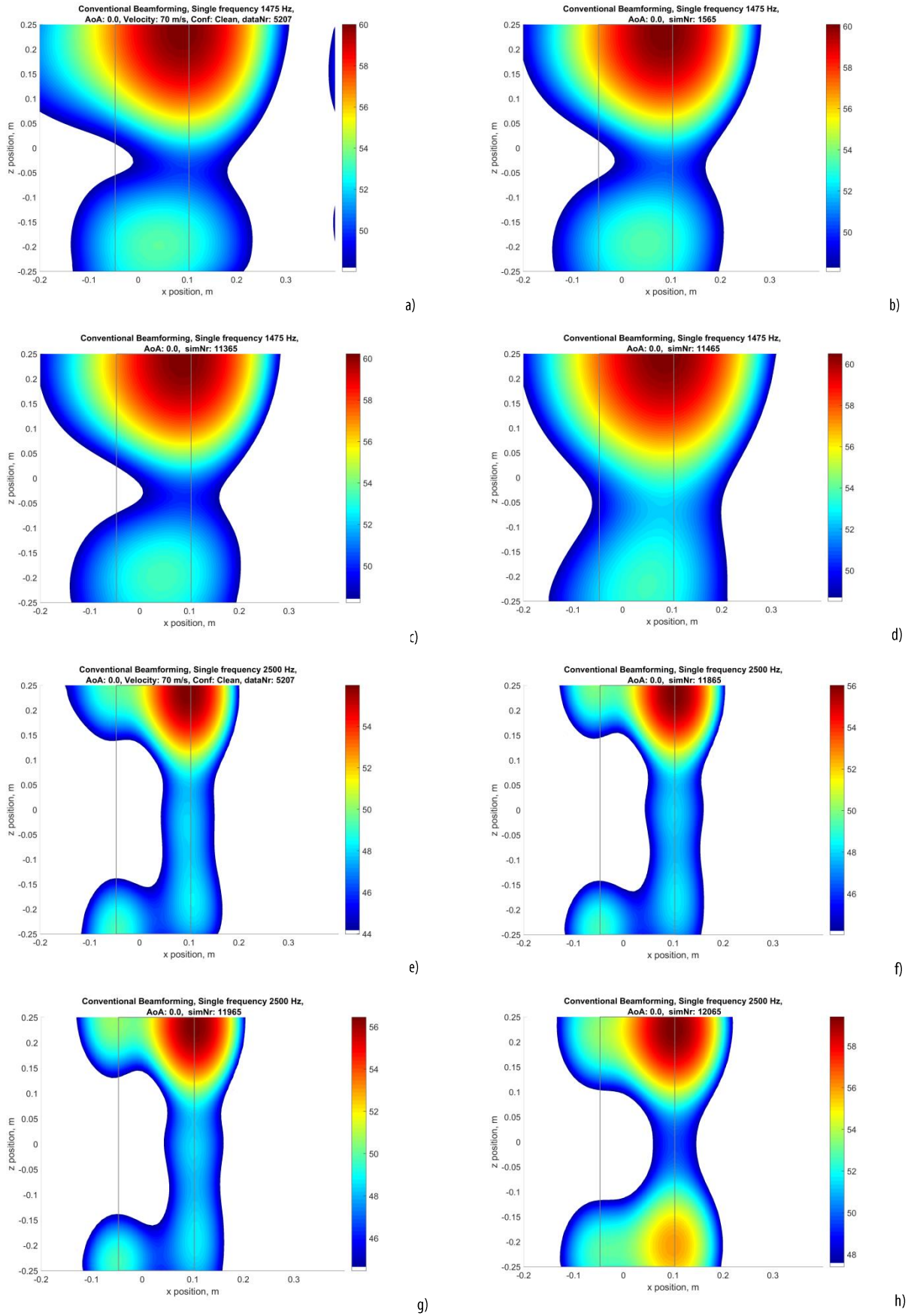


Figure 21 - Source map of real case (a) and simulated regression fits obtained with normal weighting (b), equalized weighting (c), inversed weighting (d) for 1475 Hz and similar for 2500 Hz (e, f, g and h)

Clean map, AoA: 0.0, Velocity: 70 m/s, Conf: Clean, dataNr: 5207

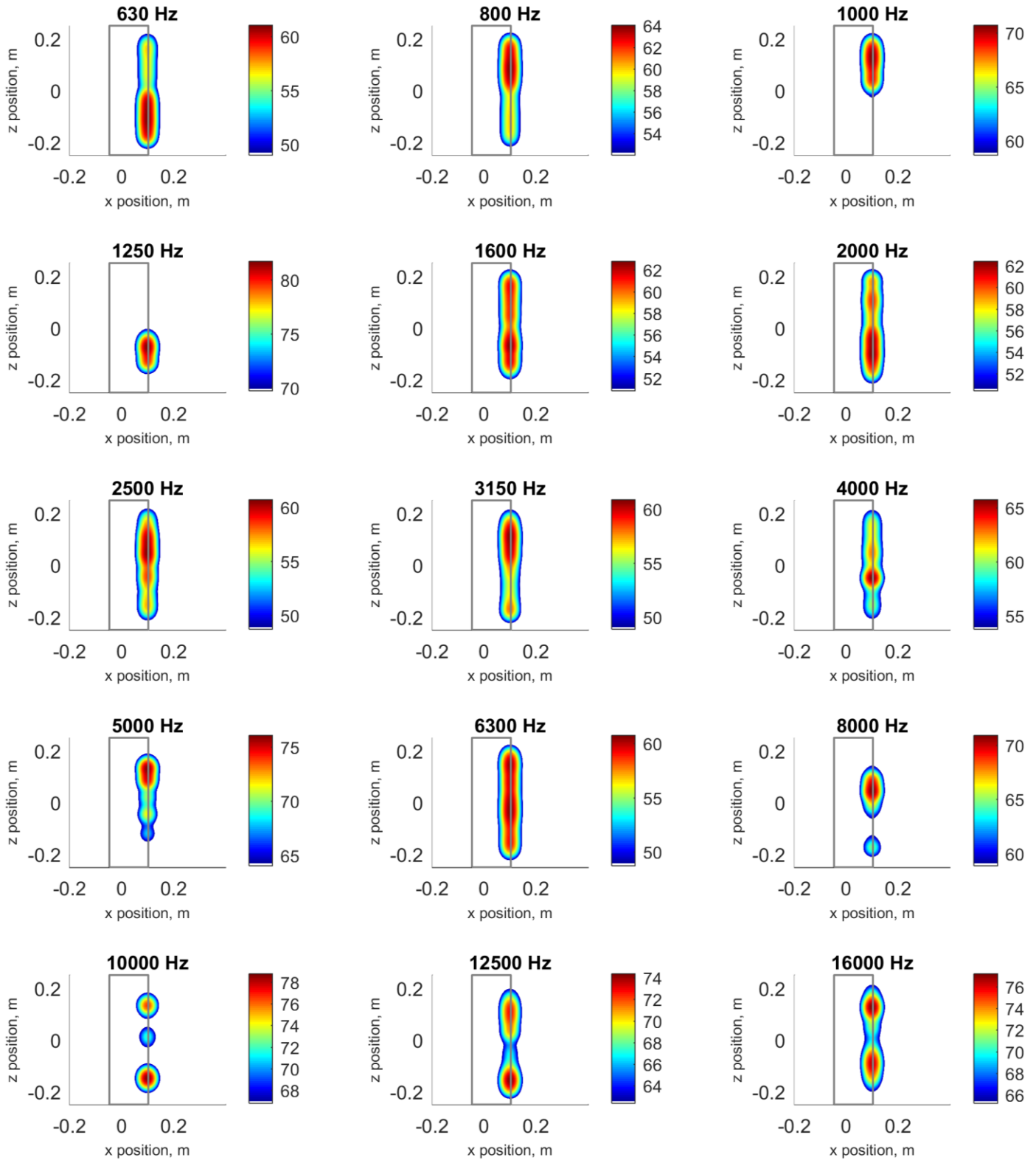


Figure 22 - CLEAN source maps of third octave band data

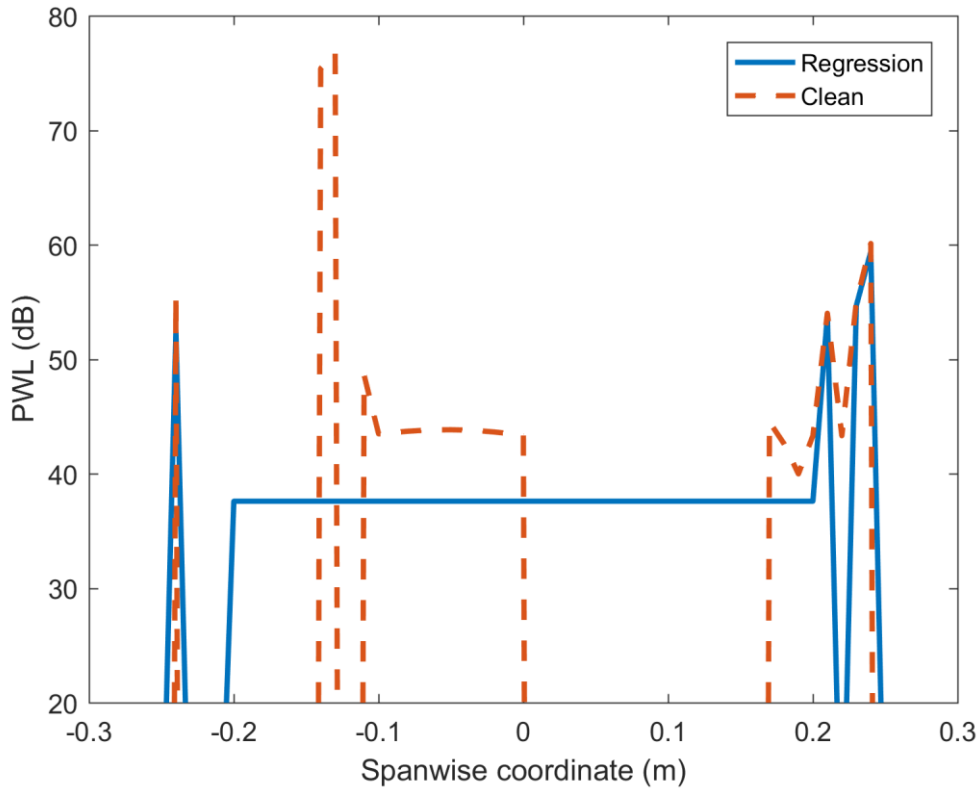


Figure 23 - Trailing Edge source power distribution output for the test case at 1325 Hz for both regression and clean deconvolution step

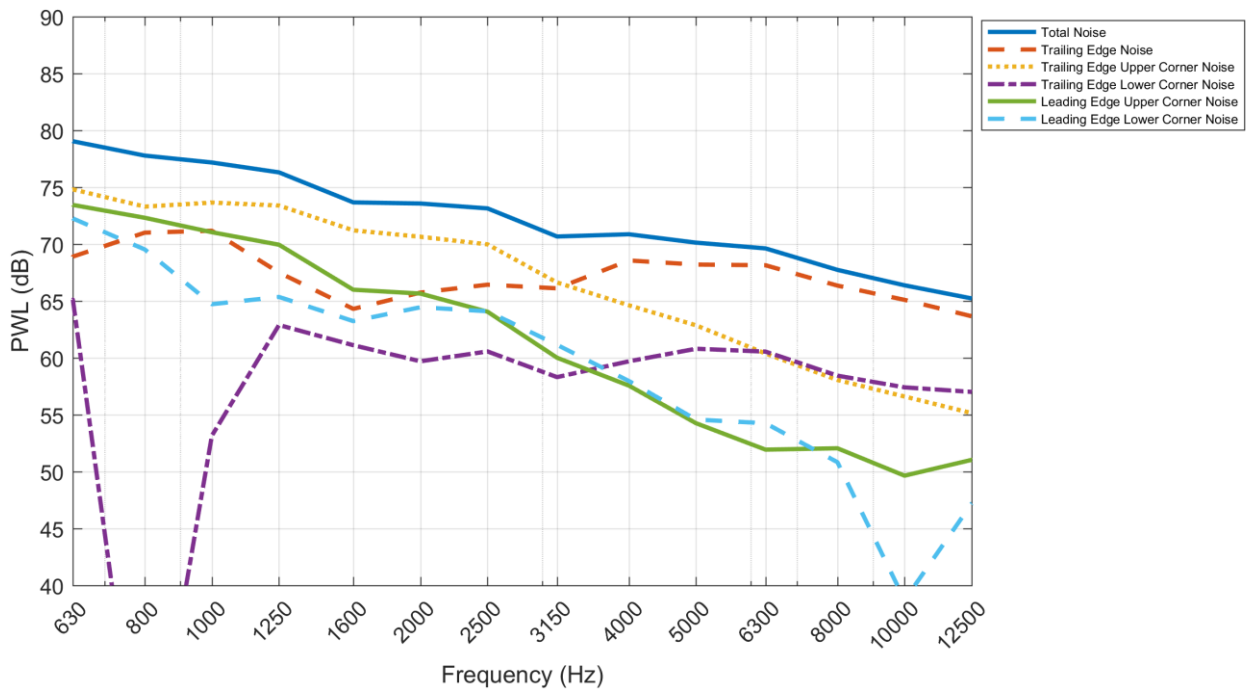


Figure 24 – Third octave noise spectra from the different noise sources for a clean configuration at 0.0 AoA and velocity 70 m/s

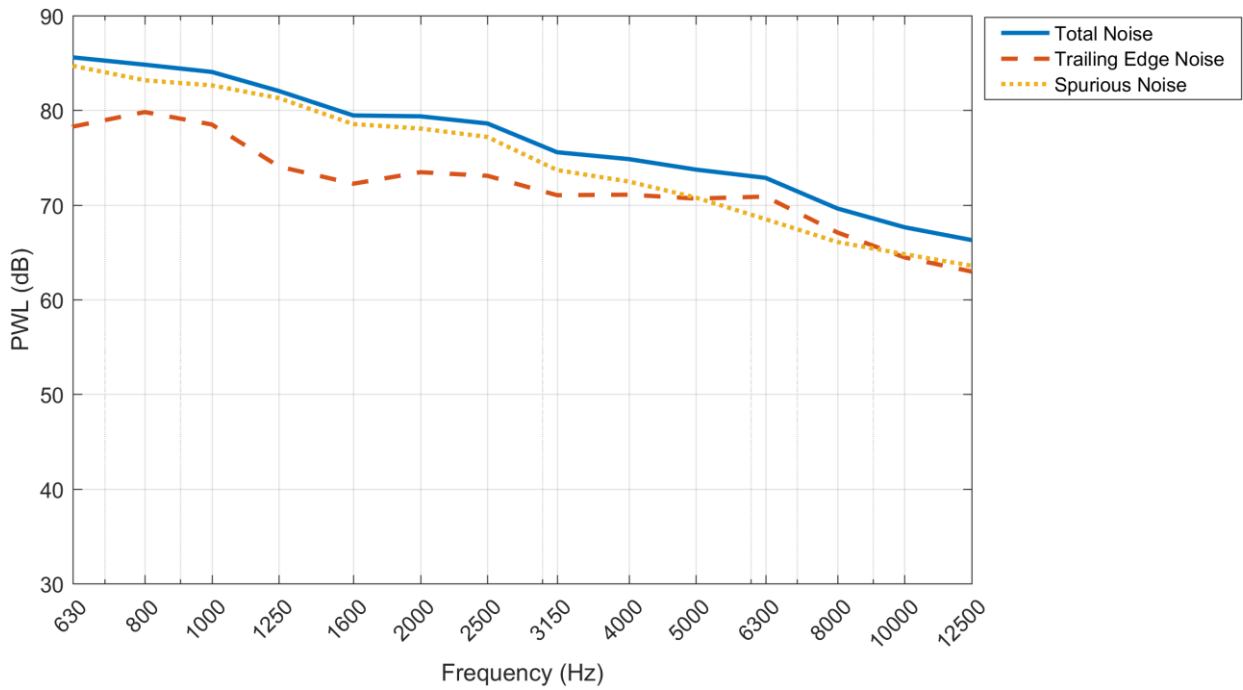


Figure 25 – Third octave noise spectra from TE and summed spurious noise sources for a clean configuration at 0.0 AoA and velocity 70 m/s

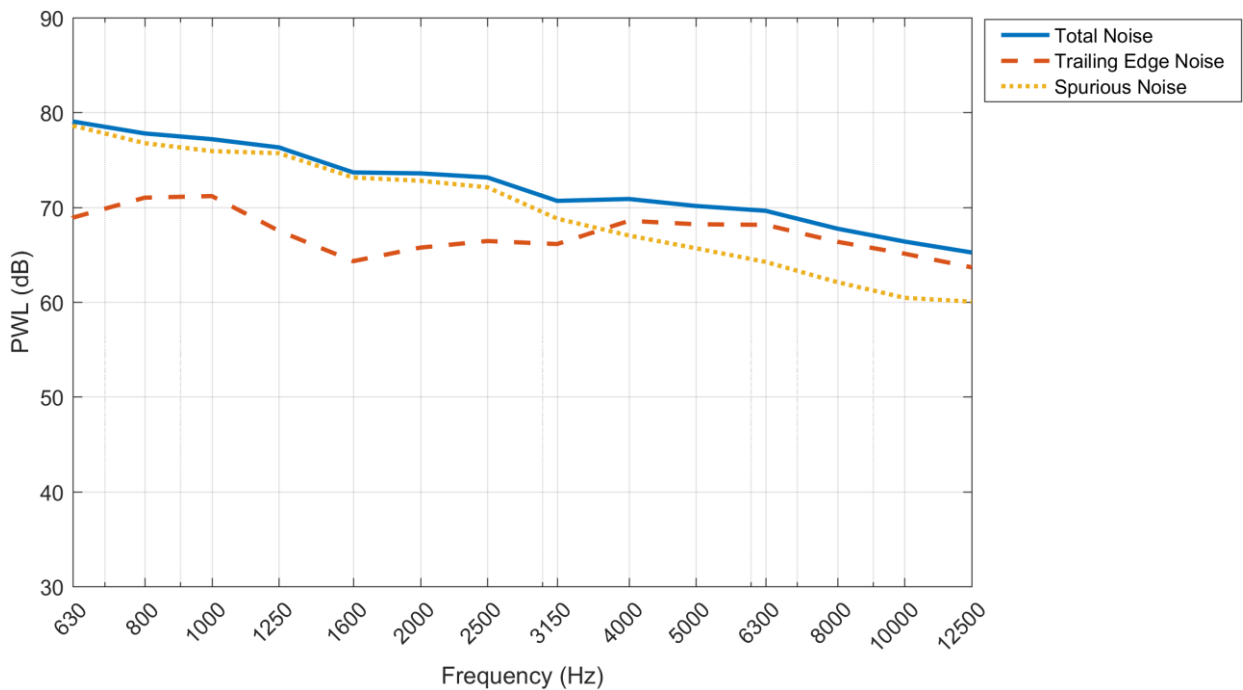


Figure 26 - Third octave noise spectra from TE and summed spurious noise sources for a clean configuration at 14.37 AoA and velocity 70 m/s

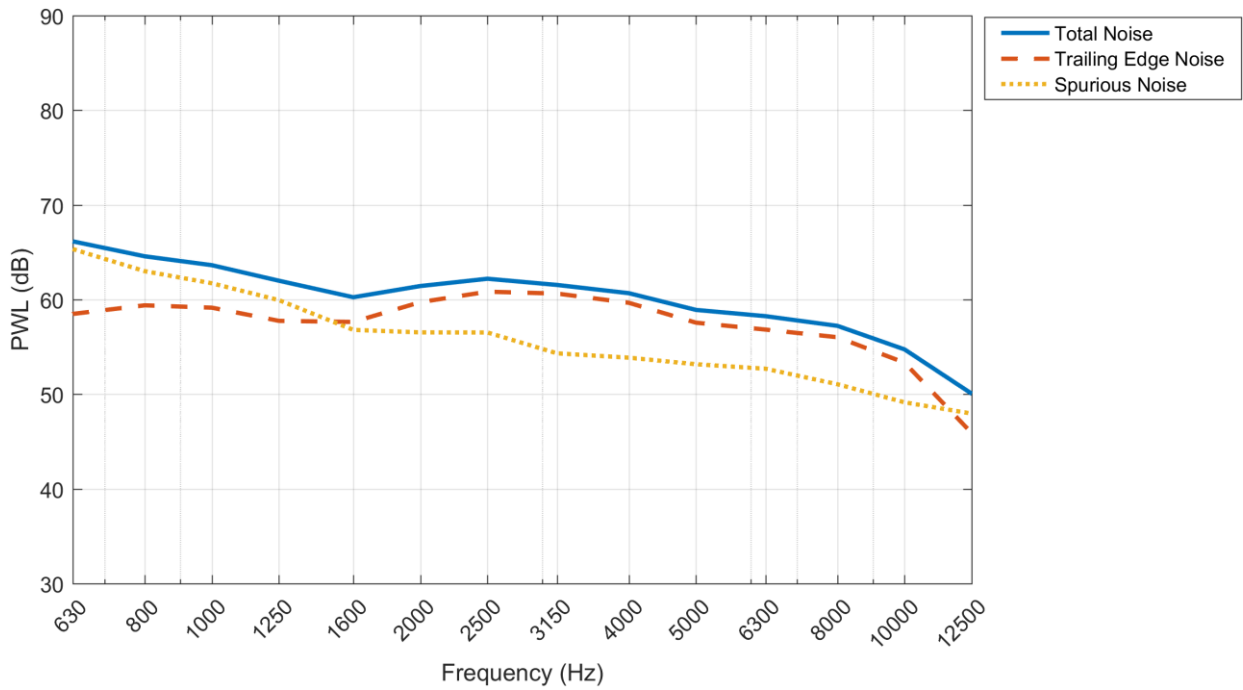


Figure 27 - Third octave noise spectra from TE and spurious noise sources for a clean configuration at 0.0 AoA and velocity 40 m/s

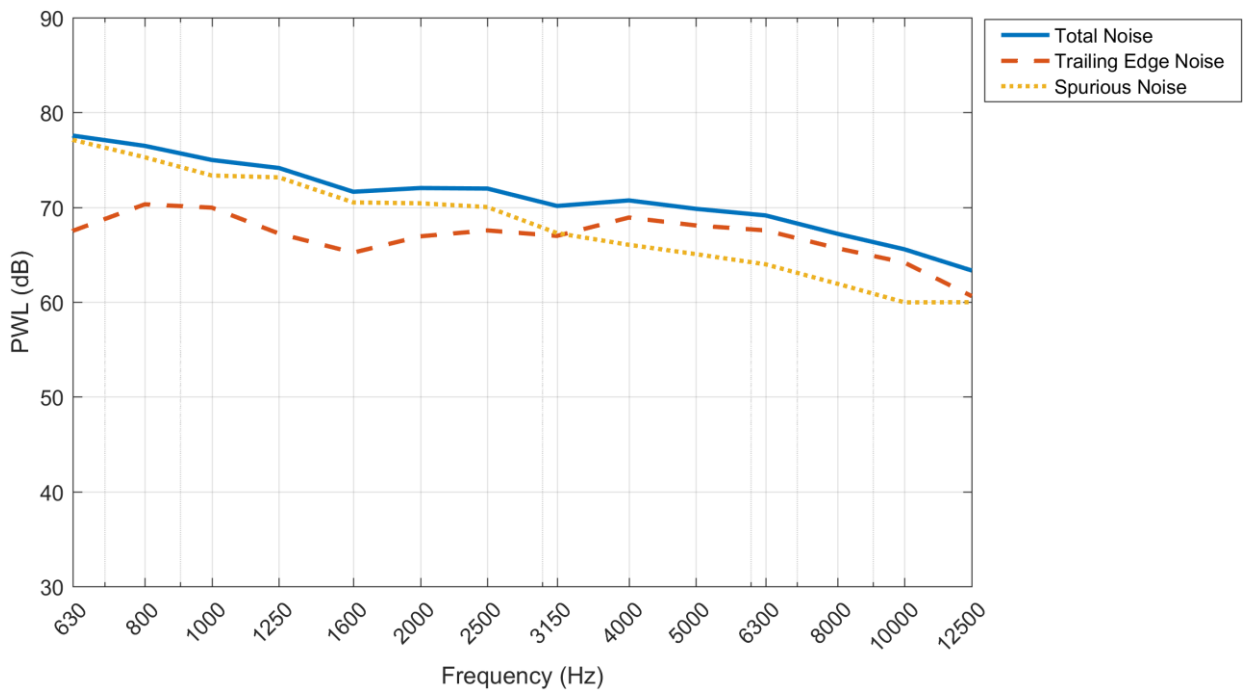


Figure 28 - Third octave noise spectra from TE and spurious noise sources for a configuration with FS at 0.0 AoA and velocity 70 m/s

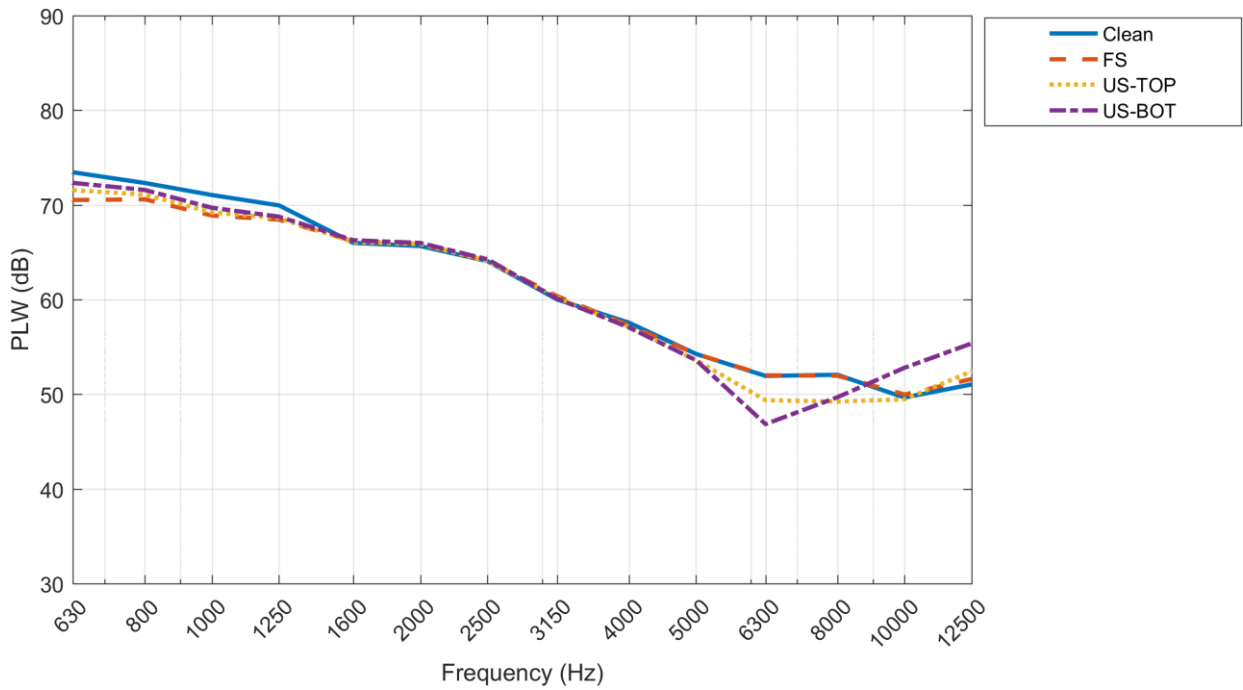


Figure 29 – Third octave noise spectra of the upper LE corner noise source at 0.0 AoA and velocity 70 m/s

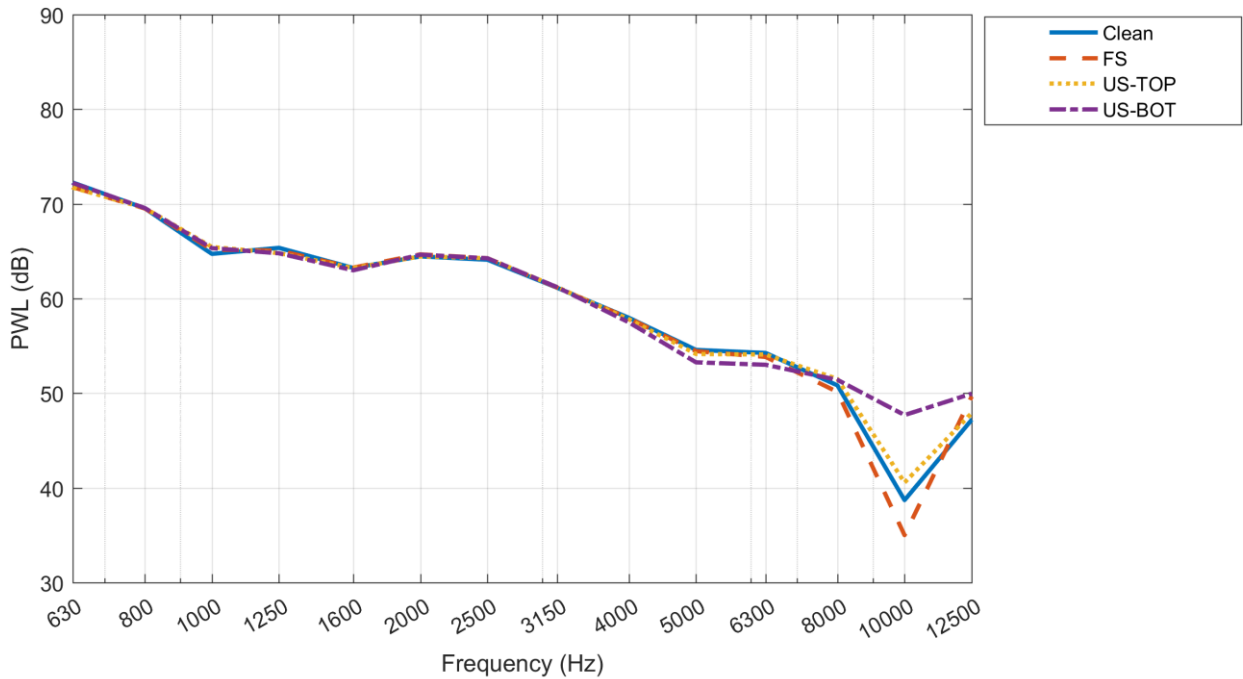


Figure 30 - Third octave noise spectra of the lower LE corner noise source at 0.0 AoA and velocity 70 m/s

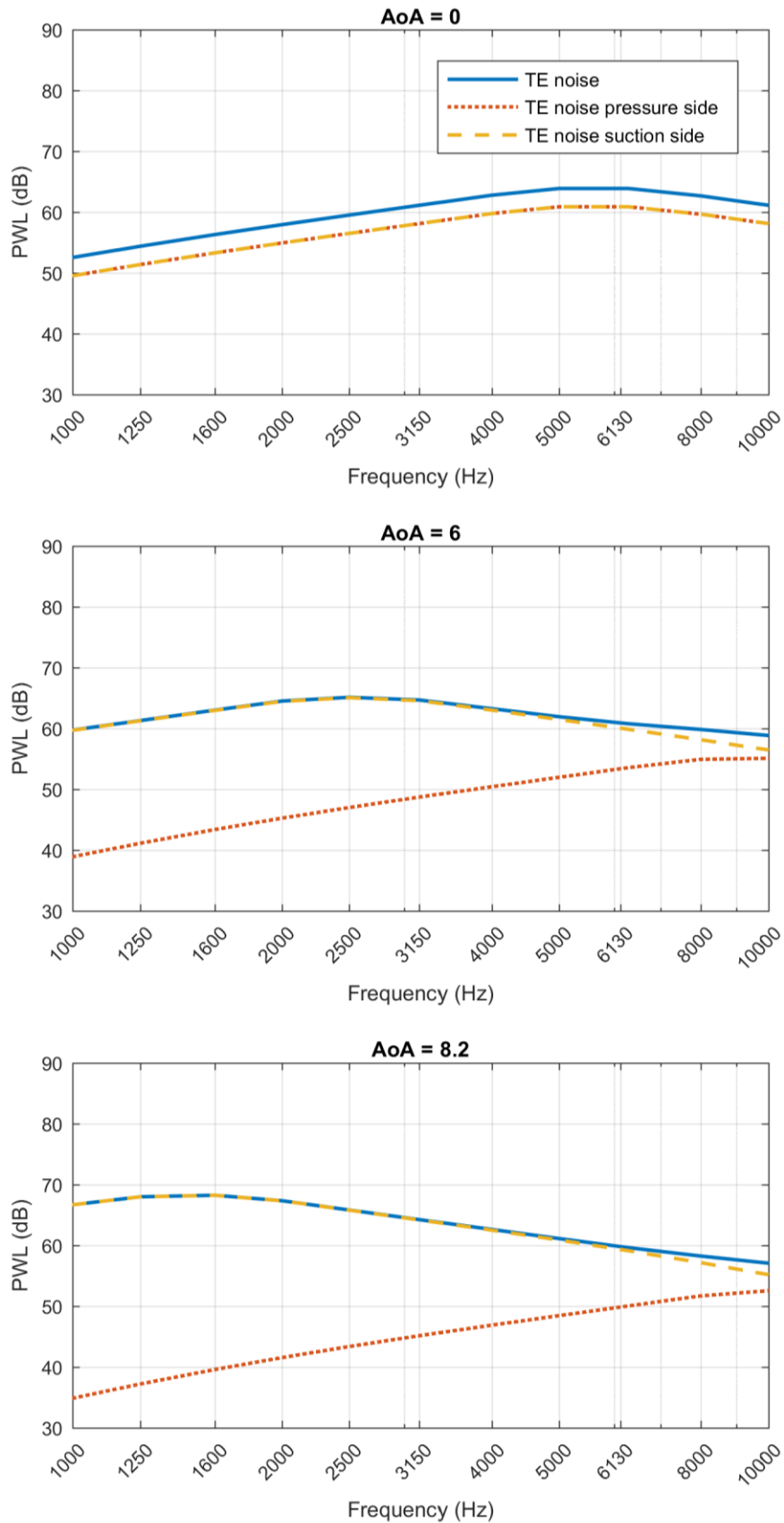


Figure 31 - TE noise spectra originated from pressure and suction side for a simulated NACA 0012 profile

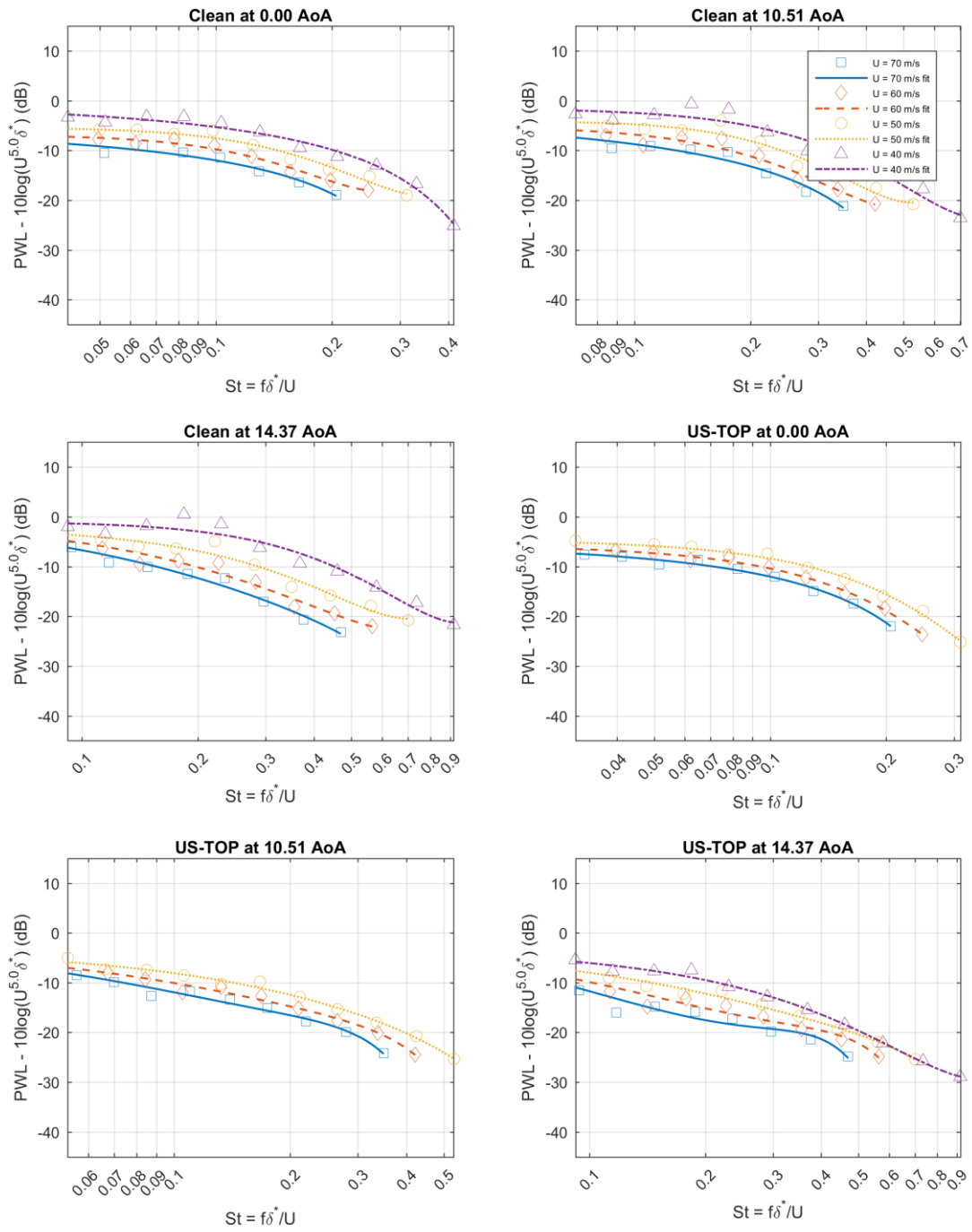


Figure 32 – Velocity scaled noise levels for different cases (part 1)

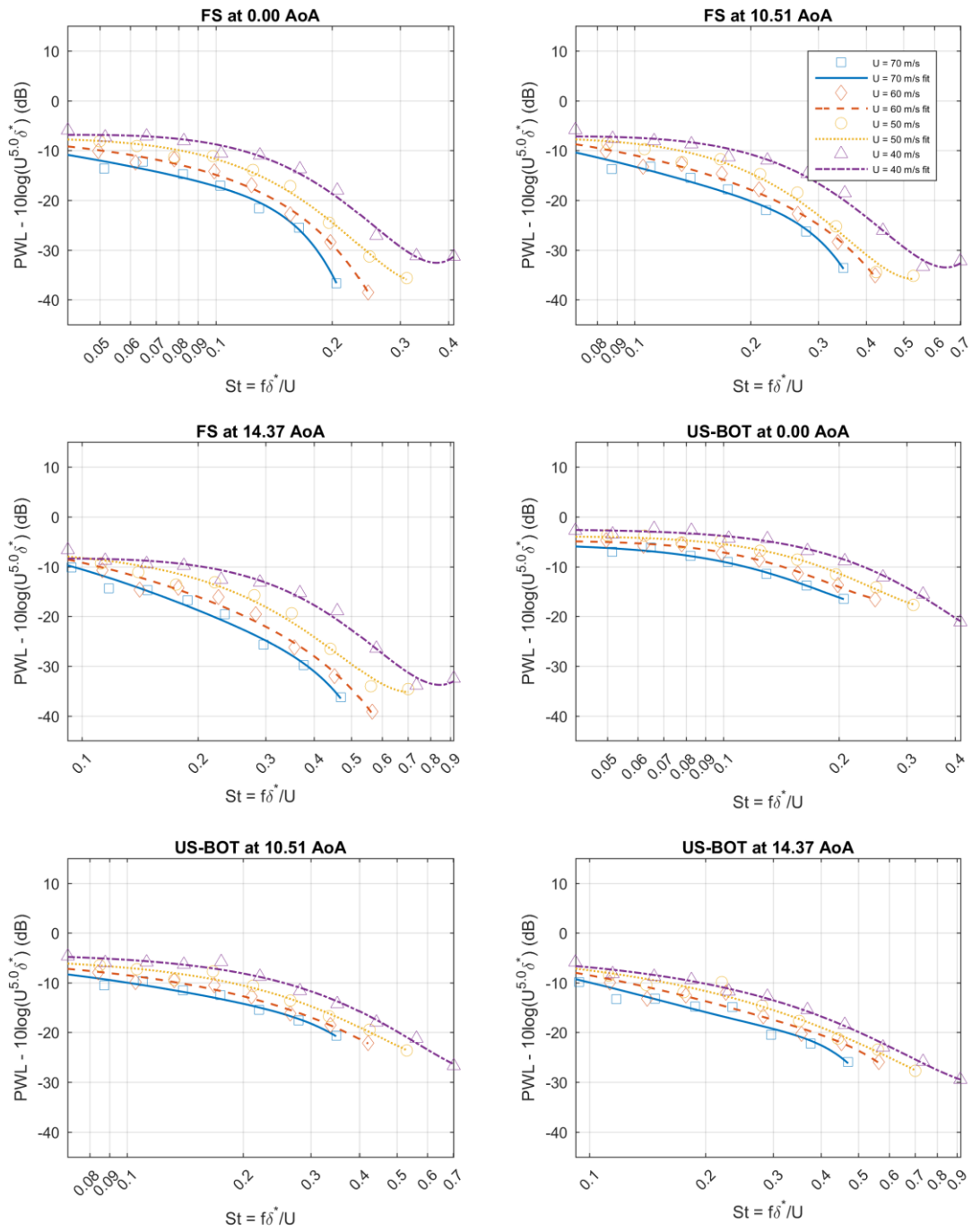


Figure 33 – Velocity scaled noise levels for different cases (part 2)

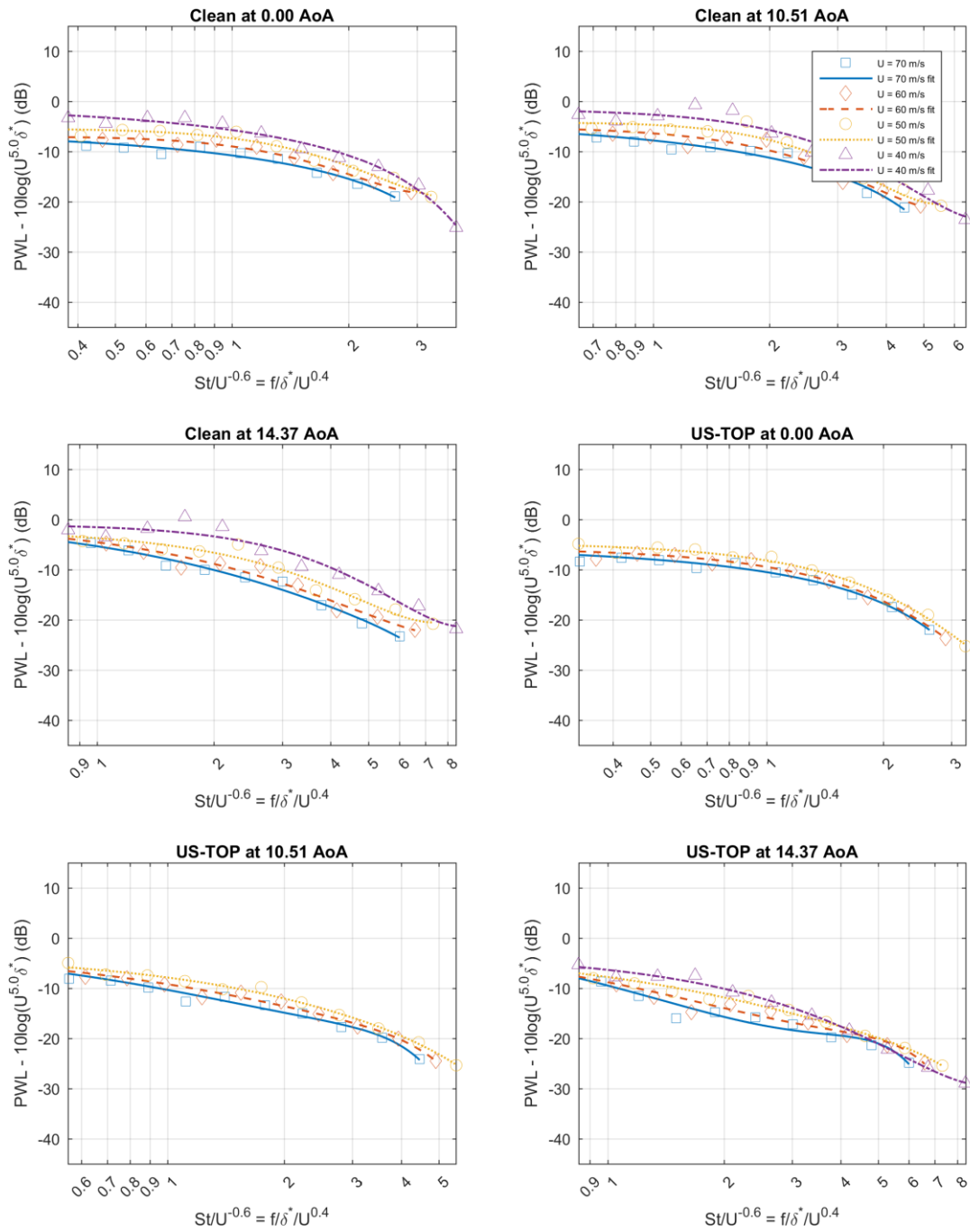


Figure 34 - Velocity scaled noise levels for different cases (part 1)

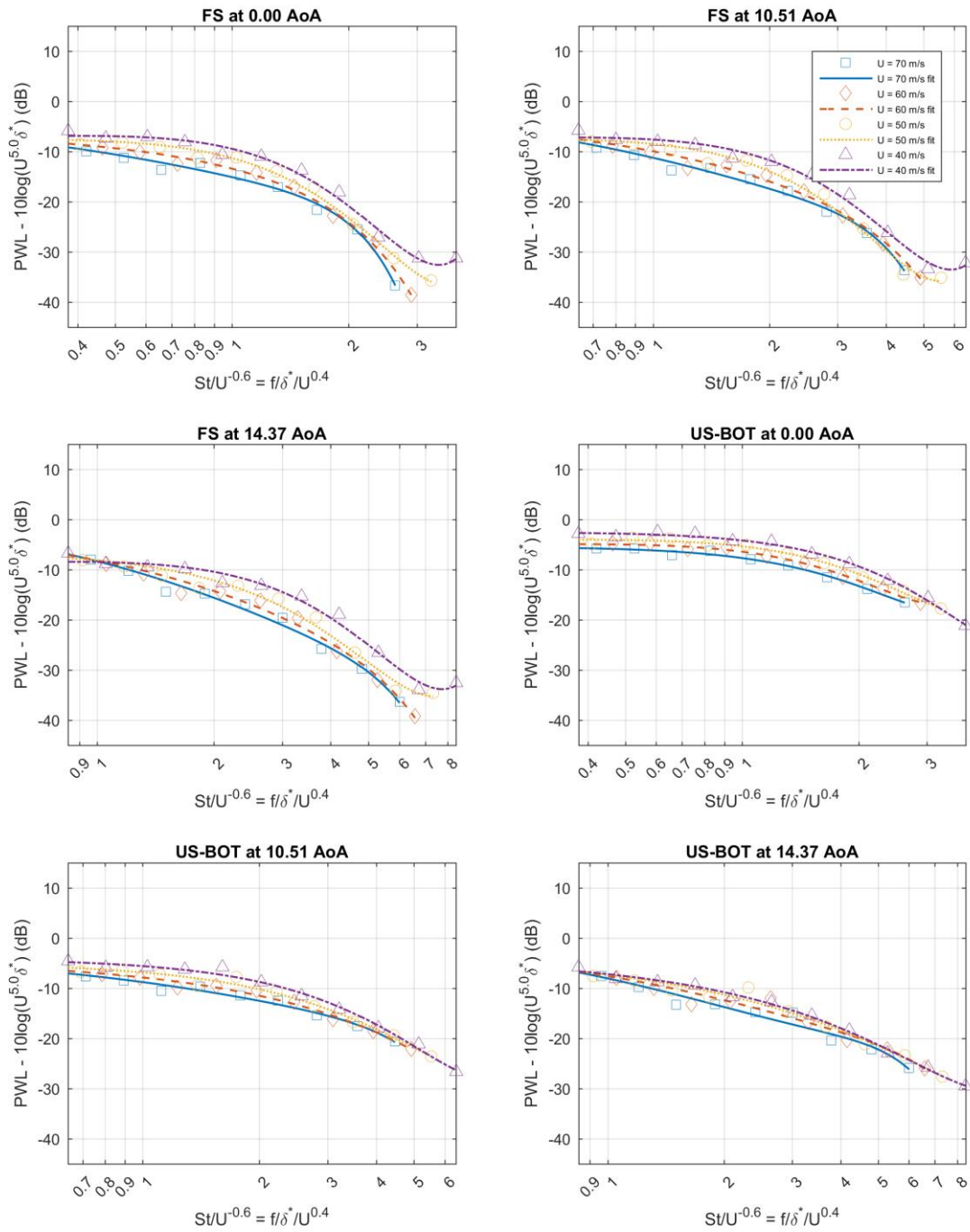


Figure 35 - Velocity scaled noise levels for different cases (part 2)

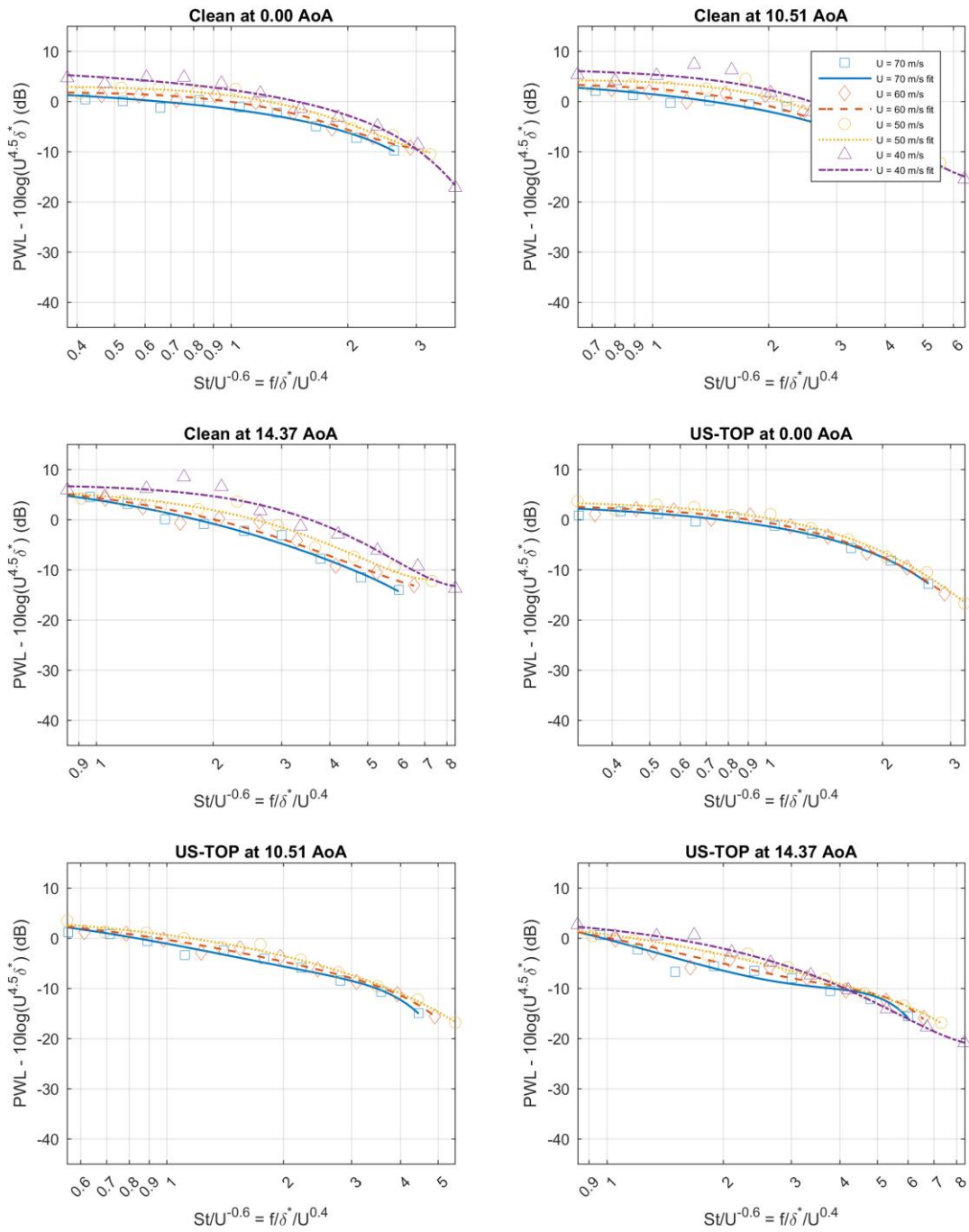


Figure 36 - Velocity scaled noise levels for different cases (part 1)

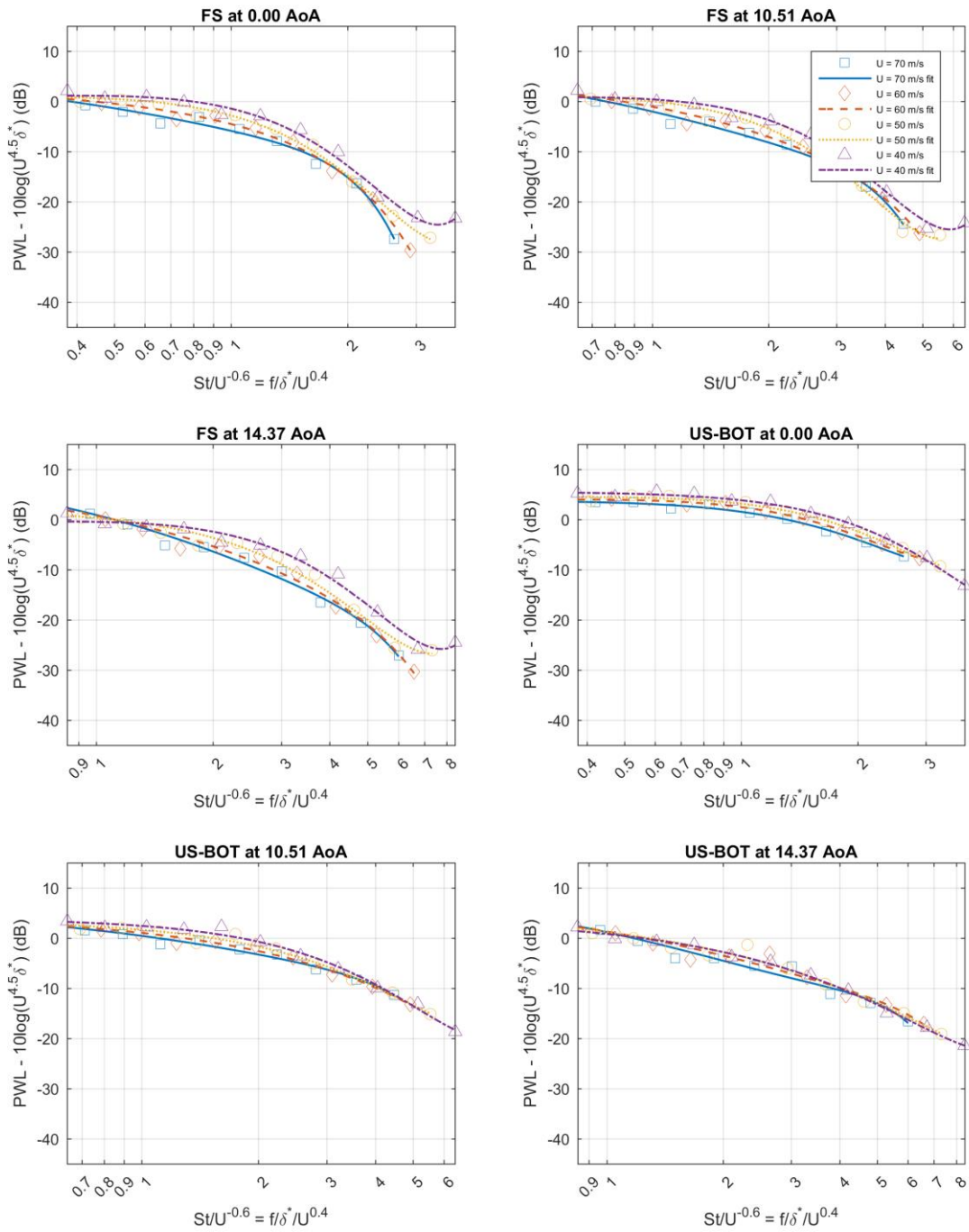


Figure 37 - Velocity scaled noise levels for different cases (part 2)

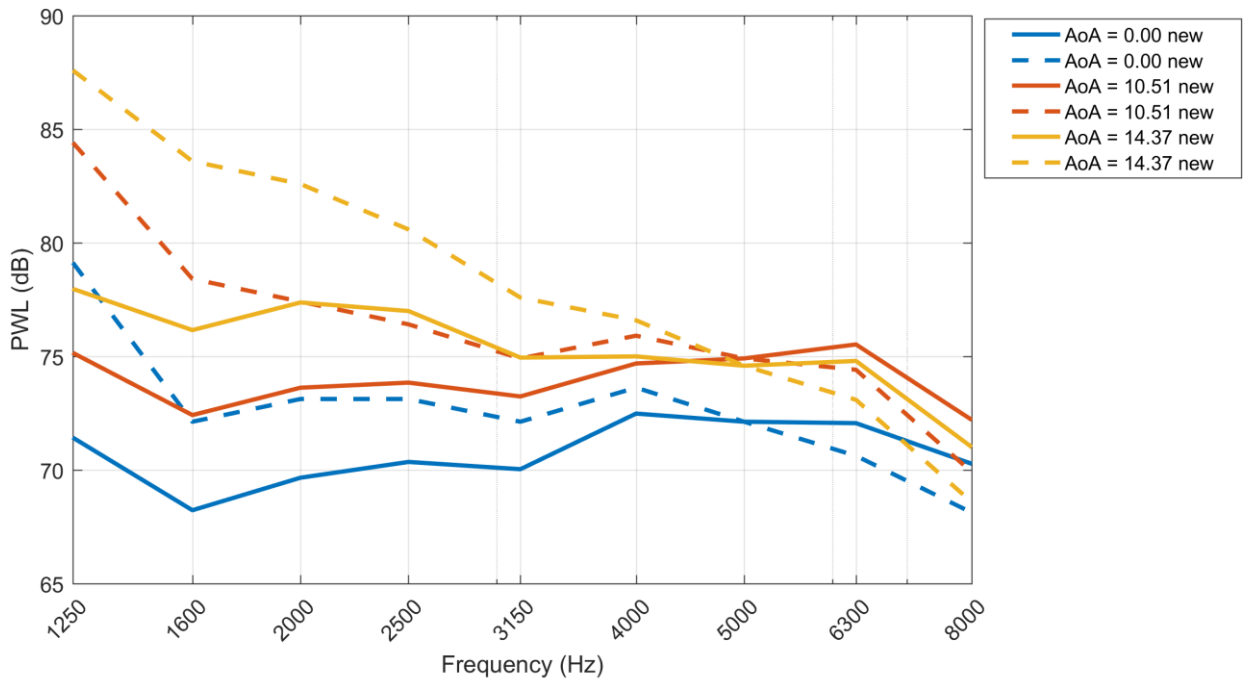


Figure 38 – Noise spectra of new obtained data compared with old obtained data for a Clean TE and velocity 70 m/s

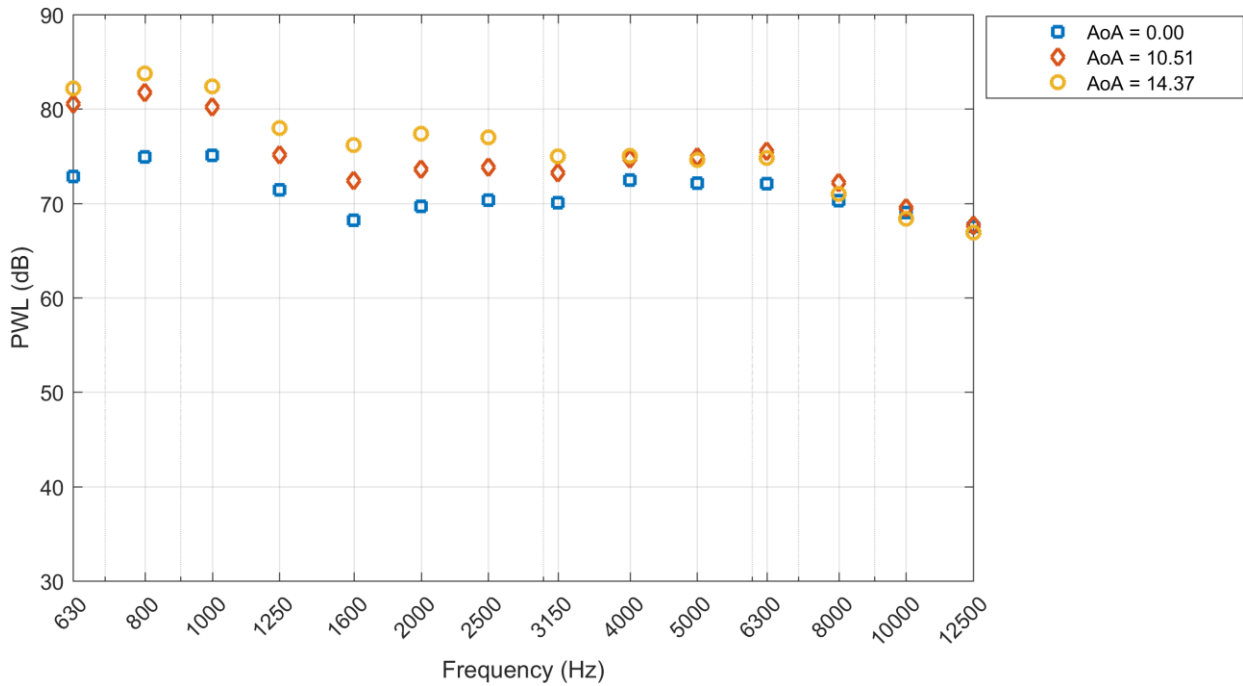


Figure 39 - Noise spectra for clean TE at 70 m/s and different AoA

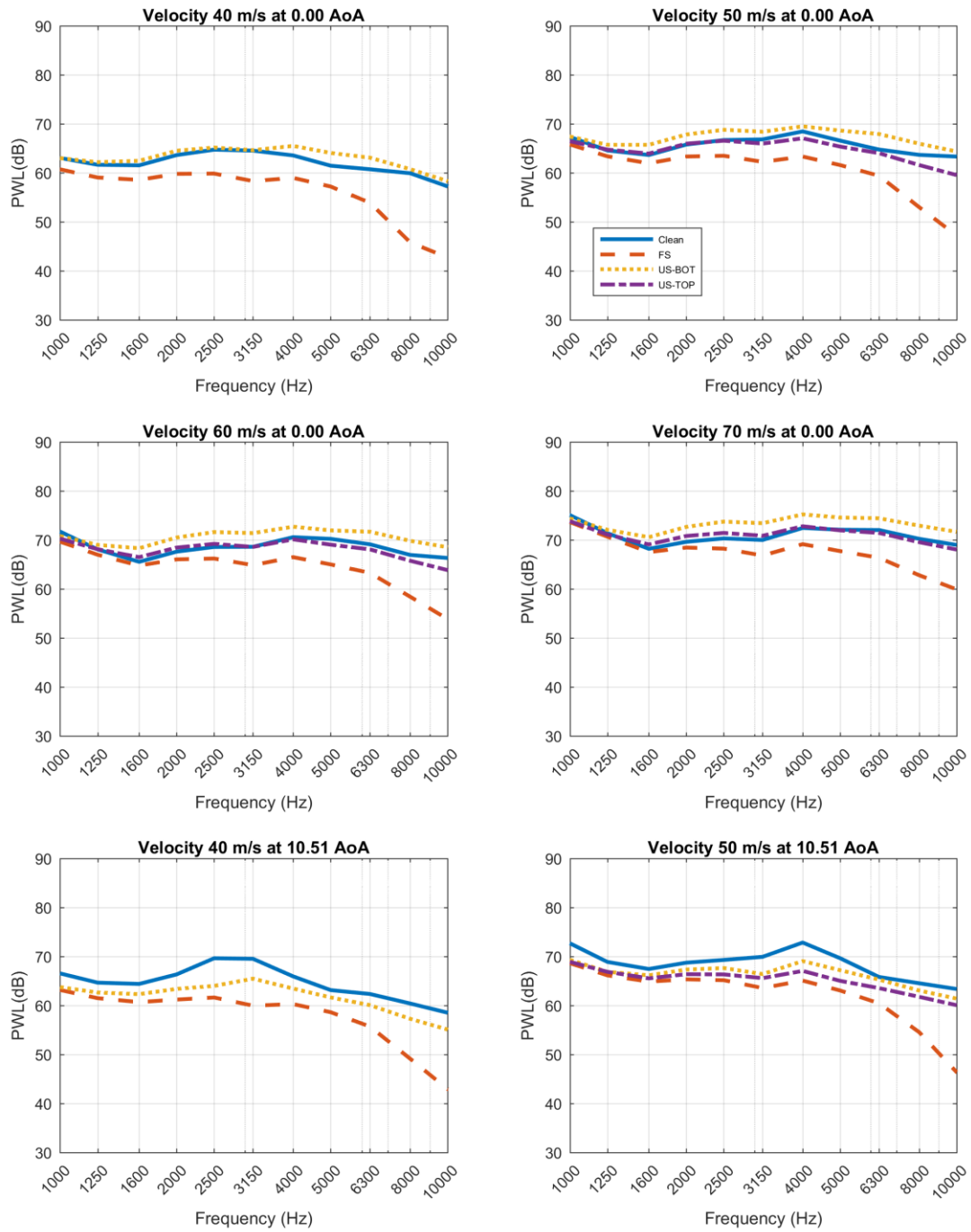


Figure 40 - Noise Spectra for different configurations compared (part 1)

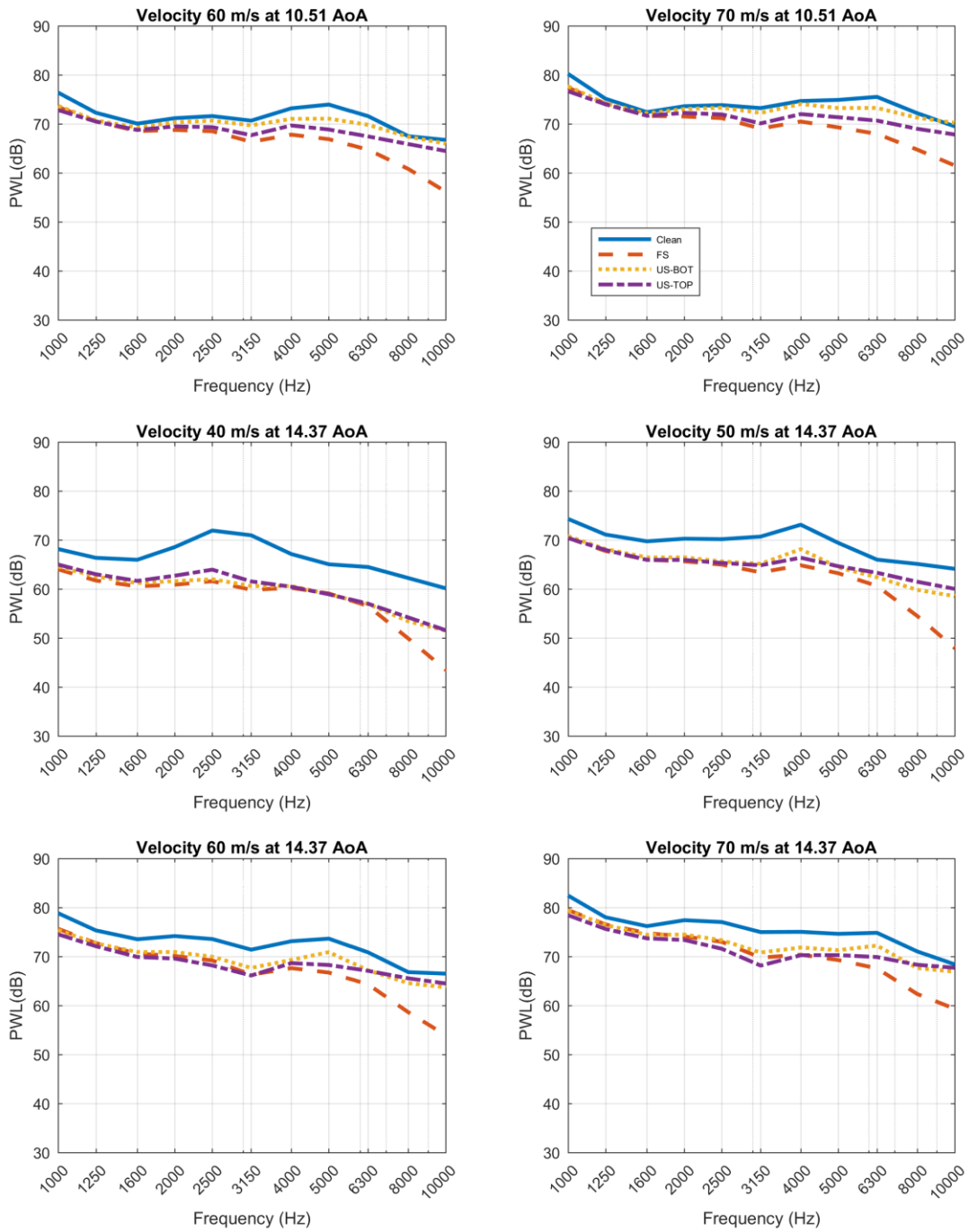


Figure 41 - Noise Spectra for different configurations compared (part 2)

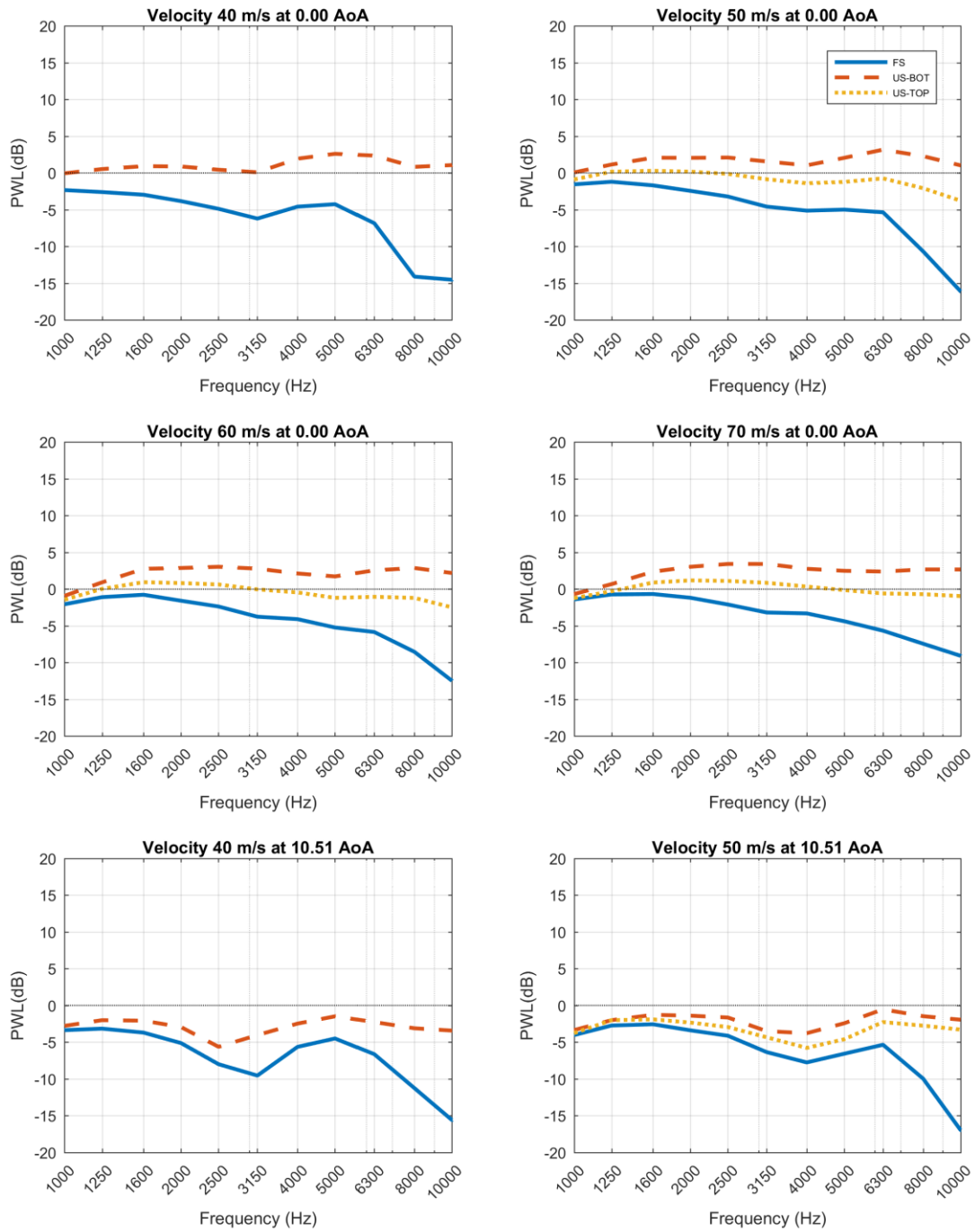


Figure 42 - Noise reduction for different serrations compared to clean TE (part 1)

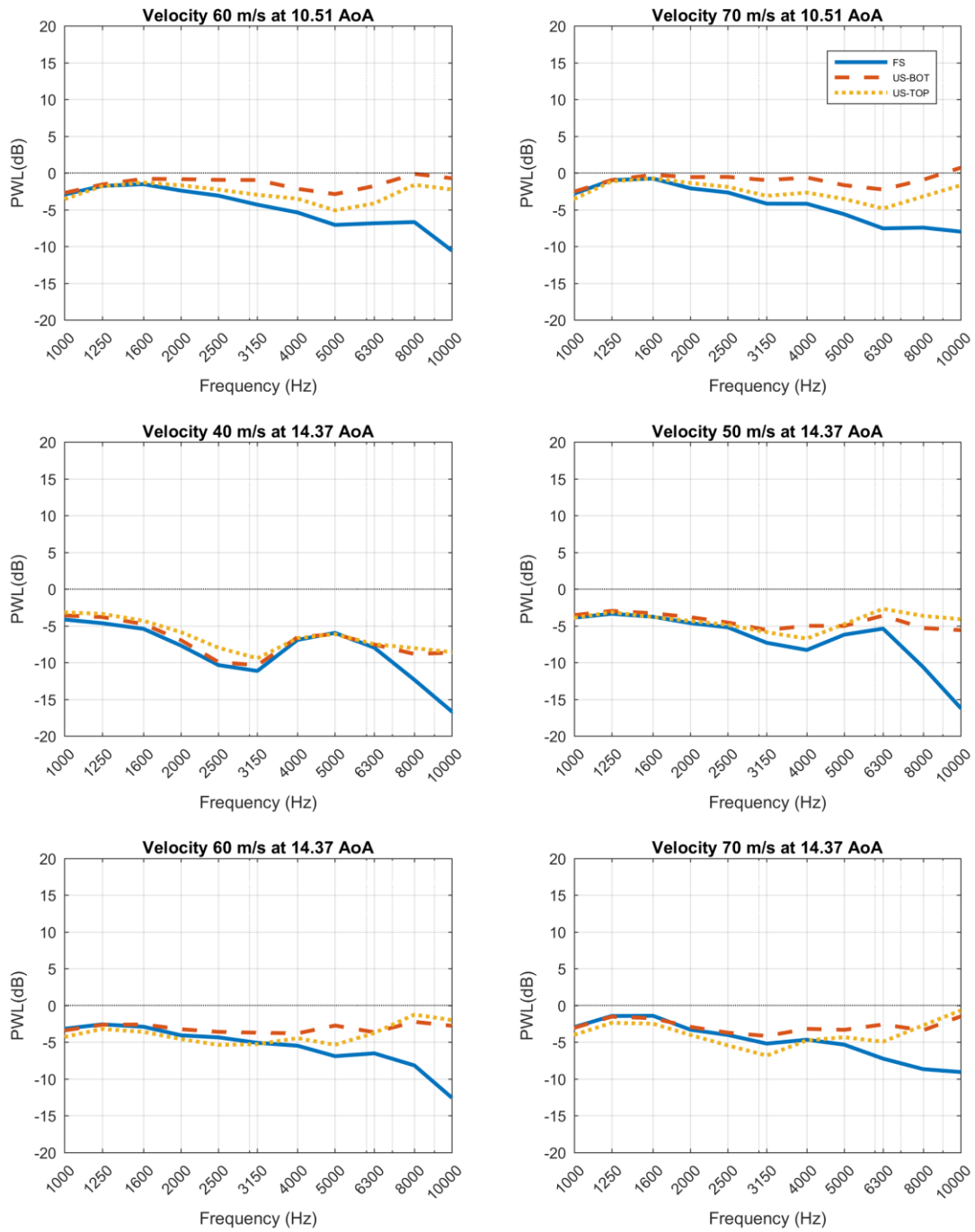


Figure 43 - Noise reduction for different serrations compared to clean (part 2)

- [1] S. Oerlemans, „Reduction of wind turbine noise using blade trailing edge devices,” in *22nd AIAA/CEAS Aeroacoustics Conference*, American Institute of Aeronautics and Astronautics, 2016.
- [2] F. S. P. M. A. M. Thomas F. Brooks, „Airfoil Self-Noise and Prediction,” 1989.
- [3] M. S. Howe, „Aerodynamic noise of a serrated trailing edge,” *Journal of Fluids and Structures*, vol. 5, nr. 1, pp. 33-45, 1991.
- [4] M. S. Howe, „Noise produced by a sawtooth trailing edge,” *The Journal of the Acoustical Society of America*, 1991.
- [5] L. Ji, W. Qiao, F. Tong, K. Xu en W. Chen, „Experimental and numerical study on noise reduction mechanisms of the airfoil with serrated trailing edge,” in *20th AIAA/CEAS Aeroacoustics Conference*, American Institute of Aeronautics and Astronautics, 2014.
- [6] M. Gruber, P. Joseph en T. P. Chong, „Experimental Investigation of Airfoil Self Noise and Turbulent Wake Reduction by the use of Trailing Edge Serrations,” in *16th AIAA/CEAS Aeroacoustics Conference*, American Institute of Aeronautics and Astronautics, 2010.
- [7] M. Gruber, P. Joseph en T. Chong, „On the mechanisms of serrated airfoil trailing edge noise reduction,” in *17th AIAA/CEAS Aeroacoustics Conference (32nd AIAA Aeroacoustics Conference)*, American Institute of Aeronautics and Astronautics, 2011.
- [8] T. P. Chong, P. Joseph en M. Gruber, „An Experimental Study of Airfoil Instability Noise with Trailing Edge Serrations,” in *16th AIAA/CEAS Aeroacoustics Conference*, American Institute of Aeronautics and Astronautics, 2010.
- [9] T. P. Chong, A. Vathylakis, P. F. Joseph en M. Gruber, „Self-Noise Produced by an Airfoil with Nonflat Plate Trailing-Edge Serrations,” *AIAA Journal*, vol. 51, nr. 11, pp. 2665-2677, #jun# 2013.
- [10] K. A. Braun, A. Gordner, N. J. C. M. v.d. Borg, A. G. M. Dassen, F. Doorenspleet en R. Parchen, „Serrated Trailing Edge Noise (STENO),” 1998.
- [11] M. Tuinstra en P. Sijtsma, „Suppression of spurious noise sources in airfoil self-noise measurements,” in *21st AIAA/CEAS Aeroacoustics Conference*, American Institute of Aeronautics and Astronautics, 2015.
- [12] K. Ehrenfried en L. Koop, „A Comparison of Iterative Deconvolution Algorithms for the Mapping of Acoustic Sources,” in *12th AIAA/CEAS Aeroacoustics Conference (27th AIAA Aeroacoustics Conference)*, American Institute of Aeronautics and Astronautics, 2006.
- [13] P. Sijtsma, „CLEAN Based on Spatial Source Coherence,” in *13th AIAA/CEAS Aeroacoustics Conference (28th AIAA Aeroacoustics Conference)*, American Institute of Aeronautics and Astronautics, 2007.
- [14] D. E. Faleiros, „Wind tunnel Investigation on Trailing Edge Noise Mitigation via Sawtooth Serrations,” 2014.
- [15] P. Sijtsma, „Elements of acoustic array data processing,” 2014.
- [16] R. P. Dougherty, „Functional Beamforming for Aeroacoustic Source Distributions,” in *20th AIAA/CEAS Aeroacoustics Conference*, American Institute of Aeronautics and Astronautics, 2014.

[17] F. V. Hutcheson en T. F. Brooks, „Effects of Angle of Attack and Velocity on Trailing Edge Noise,” *International Journal of Aeroacoustics*, 2006.

7 References

NLR

Anthony Fokkerweg 2

1059 CM Amsterdam, The Netherlands

[p](#)) +31 88 511 3113 [f](#)) +31 88 511 3210